The Astrophysical Journal Supplement Series, 288:5 (17pp), 2027 January https://doi.org/10.3847/1538-4365/aeb300
© 2026. The Author(s). Published by the American Astronomical Society.
OPEN ACCESS

Persistent Sub-MeV Ion Enhancement Downstream of an Interplanetary Shock: Multispacecraft Observations near L1

L.-L. Zhao[1,2,13], X. Zhu[1], Y. Jiao[2], Z. Jin[2], N. M. Subashchandar[1], G. P. Zank[1,2], A. Silwal[3], D. J. McComas[3], M. I. Desai[4], S. Raptis[5], J. Giacalone[6], M. A. Dayeh[4], M. J. Starkey[4], K. Ogasawara[4], S. T. Hart[4], M. E. Cuesta[3], L. Y. Khoo[3], D. Turner[5], J. S. Rankin[3], T. S. Horbury[7], S. A. Livi[8], E. R. Christian[9], J. G. Mitchell[9], M. Gkioulidou[10], R. B. Torbert[11], and D. Vassiliadis[12]

[1] Center for Space Plasma and Aeronomic Research (CSPAR), The University of Alabama in Huntsville, Huntsville, AL 35805, USA; lz0009@uah.edu
[2] Department of Space Science, The University of Alabama in Huntsville, Huntsville, AL 35805, USA
[3] Department of Astrophysical Sciences, Princeton University, Princeton, NJ 08544, USA
[4] Southwest Research Institute, San Antonio, TX 78238, USA
[5] Applied Physics Laboratory, Johns Hopkins University, Laurel, MD 20723, USA
[6] Lunar and Planetary Laboratory, University of Arizona, Tucson, AZ 85721, USA
[7] Imperial College London, London, SW7 2AZ, UK
[8] Department of Climate and Space Sciences and Engineering, University of Michigan, Ann Arbor, MI 48109, USA
[9] NASA Goddard Space Flight Center, Greenbelt, MD 20771, USA
[10] Applied Physics Laboratory, The Johns Hopkins University, Laurel, MD 20723, USA
[11] Space Science Center, University of New Hampshire, Durham, NH, USA
[12] National Oceanographic and Atmospheric Administration NESDIS Office of Space Weather Observations (SWO), Lanham, MD 20706, USA
Received 2026 September 8; revised 2026 October 7; accepted 2026 October 9; published 2026 November 4

Abstract

On 2026 February 4, an interplanetary shock crossed the L1 region and was followed about 7.7 hr later by a heliospheric current sheet/heliospheric plasma sheet (HCS/HPS), while energetic-ion intensities continued to evolve throughout the intervening downstream region. The shock was observed by IMAP, Wind, ACE, DSCOVR, and SOLAR-1, providing a multispacecraft view of its geometry. Multispacecraft timing and local shock-normal analyses show that the shock is highly quasiperpendicular but spatially nonplanar across L1. Energetic-ion intensities exhibit a pronounced energy-dependent response. Sub-MeV intensities increase well upstream of the shock and remain enhanced throughout the downstream region until approaching the HCS/HPS, whereas intensities above ∼1 MeV show a much weaker downstream enhancement and tend to peak near the shock. The energy spectra also soften downstream, with the fitted spectral break shifting from several MeV near the shock to lower energies farther downstream. Pitch-angle distributions evolve from pronounced field-aligned streaming upstream to enhanced intensities at oblique-to-perpendicular pitch angles downstream, with the anisotropy persisting through much of the downstream sheath and gradually broadening toward the HCS/HPS. A secondary current sheet embedded within the downstream HPS exhibits signatures consistent with a localized reconnection exhaust. Overall, the observations indicate that the sub-MeV ion population is strongly influenced by the shock, while its subsequent downstream evolution is shaped primarily by energy-dependent transport. Localized energization within the disturbed downstream sheath may provide an additional contribution to the sub-MeV population.

Unified Astronomy Thesaurus concepts: Solar wind (1534); Interplanetary shocks (829)

1. Introduction

Interplanetary (IP) shocks are among the most efficient particle accelerators in the heliosphere and frequently produce energetic storm particle (ESP) events. Energetic particles accelerated at coronal mass ejection (CME)-driven shocks provide an important probe of both collisionless shock physics and particle transport. Diffusive shock acceleration (DSA) and shock-drift acceleration (SDA) can accelerate ions and electrons over a broad energy range, with the acceleration efficiency depending on the shock geometry, compression ratio, and the surrounding magnetic turbulence that controls particle scattering and repeated interactions with the shock (e.g., W. I. Axford et al. 1977; A. R. Bell 1978; R. D. Blandford & J. P. Ostriker 1978; L. O. Drury 1983; J. R. Jokipii 1987; M. A. Lee 2005; J. Giacalone 2012; M. Desai & J. Giacalone 2016). In the idealized steady-state, planar DSA picture, the energetic-particle distribution decreases exponentially with distance upstream of the shock over a characteristic diffusion length, whereas the downstream distribution is approximately spatially uniform in the absence of losses or escape. However, the idealized one-dimensional, steady-state DSA model does not capture the complex geometry, magnetic environment, and temporal evolution of particle acceleration at IP shocks. Shock curvature, spatial variations in shock geometry, upstream turbulence, and changing magnetic connectivity can modify the observed energetic-particle intensity profile significantly. In addition, high-time-resolution observations show that particle acceleration at shocks can be highly dynamic, exhibiting temporal and/or spatial variations on timescales from seconds to minutes (L. Yang et al. 2023, 2024, 2025a, 2025b).

[13] Corresponding author.

Original content from this work may be used under the terms of the Creative Commons Attribution 4.0 licence. Any further distribution of this work must maintain attribution to the author(s) and the title of the work, journal citation and DOI.

Consistent with these departures from the idealized DSA picture, observations reveal considerable diversity in shock-associated energetic-particle intensity profiles. Particle intensities may peak sharply near the shock, rise gradually toward the shock, remain enhanced for extended periods downstream, or reach their maximum well after the local shock passage (D. Lario et al. 2003, 2005; L.-L. Zhao et al. 2019a). These different profiles reflect both shock acceleration and subsequent particle transport through the surrounding magnetic field. In particular, spatial variations in the shock surface and large-scale magnetic fluctuations can change the magnetic connection between an observer and different regions of the shock, allowing shock-accelerated particles to be transported and concentrated away from the local shock crossing (e.g., J. Giacalone 2012; M.-Y. Lo et al. 2026).

Beyond changes in shock connectivity, the subsequent transport of energetic particles is governed by their interactions with turbulent magnetic fields and large-scale heliospheric structures. As particles propagate away from the shock, they undergo pitch-angle scattering, spatial diffusion, convection with the solar wind, and adiabatic energy changes (E. N. Parker 1965; J. R. Jokipii 1966; D. Ruffolo 1995; M. Zhang et al. 2009). Magnetic turbulence controls particle scattering and diffusion and can also contribute to particle energization under certain conditions (J. R. Jokipii 1966; W. H. Matthaeus et al. 2003; L. A. Fisk & G. Gloeckler 2007; V. Petrosian 2012). In addition, large-scale magnetic structures, including the heliospheric current sheet (HCS), corotating interaction regions (CIRs), and magnetic flux ropes, can modify energetic-particle transport by changing magnetic connectivity, cross-field transport, and redistributing energetic particles over extended spatial and temporal scales (O. Khabarova et al. 2015; L.-L. Zhao et al. 2018, 2019b; J. Giacalone et al. 2021; N. Dresing et al. 2023; A. Silwal et al. 2024; Z. Ding et al. 2025; X. Zhu et al. 2026).

Among these structures, the HCS is of particular interest because it represents a large-scale reversal of the magnetic-field polarity and is occasionally associated with magnetic reconnection (J. T. Gosling et al. 2005b, 2006; T. D. Phan et al. 2021; M. Ala-Lahti et al. 2025). Enhancements of suprathermal and energetic particles have been reported in association with HCS crossings (L. Adhikari et al. 2019; E. K. J. Kilpua et al. 2021; M. I. Desai et al. 2022, 2025), with the most pronounced signatures often occurring at relatively low energies, typically below $\sim$1 MeV nuc^{-1}. A variety of processes have been proposed to account for these enhancements, including transport along meandering magnetic field lines, particle trapping within current-sheet structures, stochastic acceleration in contracting magnetic islands, and reconnection-related compression and energization (J. F. Drake et al. 2006; M. Oka et al. 2010; V. V. Zharkova & O. V. Khabarova 2012; G. P. Zank et al. 2014, 2015; J. A. le Roux et al. 2015; G. Murtas et al. 2024). The efficiency and relative importance of these processes are expected to depend on heliocentric distance and the surrounding solar-wind environment. Near 1 au, local HCS reconnection generally provides less magnetic energy per particle than in the near-Sun solar wind, making direct acceleration to hundreds of keV energies less favorable (J. T. Gosling et al. 2005a; T. D. Phan et al. 2021; S. Du et al. 2025). Nevertheless, as a large-scale magnetic-sector boundary, the HCS can still substantially modify the transport and spatial distribution of energetic particles (M. Battarbee et al. 2018; K. Liou & C.-C. Wu 2024).

The role of the HCS may become particularly important when it is overtaken by a fast-propagating IP shock. Numerical MHD simulations have shown that shock–HCS interactions can compress and distort the HCS and modify the local magnetic-field configuration (e.g., D. Odstrčil et al. 1996; Z. Smith et al. 1998). Within the compressed downstream region, the disturbed current sheet may develop secondary current sheets, magnetic islands, and localized reconnection sites (O. Khabarova et al. 2015; O. Malandraki et al. 2019; M. Ala-Lahti et al. 2025), providing additional opportunities for particle trapping and localized energization (J. Giacalone & D. Burgess 2010; G. P. Zank et al. 2015; J. A. le Roux et al. 2016; C.-C. Wu et al. 2016; G. Murtas et al. 2024). Meanwhile, changes in field line topology across the HCS can change magnetic connectivity and redistribute shock-accelerated particles. Thus, the shock–HCS configuration may influence energetic particles through both the shock-generated particle population and subsequent modifications of particle transport, with the possibility of additional localized energization.

In this paper, we investigate an IP shock that crossed the L1 region on 2026 February 4 (M. E. Cuesta et al. 2026) and was followed approximately 7.7 hr later by an HCS crossing, using coordinated multispacecraft observations. The analysis characterizes the shock geometry and large-scale structure of the shock front, followed by an examination of the energetic-ion time–intensity profiles, pitch-angle distributions (PADs), and energy spectra throughout the event. The HCS crossing is also analyzed for signatures of localized magnetic reconnection. The implications of these observations for shock acceleration, subsequent particle transport, and the sustained downstream low-energy ion enhancement are then discussed.

2. Data and Shock Geometry

The recently launched IMAP mission (D. J. McComas et al. 2025), together with Wind (L. B. Wilson et al. 2021), ACE (E. C. Stone et al. 1998), DSCOVR (J. Burt & B. Smith 2012), and Space Weather Observations at L1 to Advance Readiness 1 (SOLAR-1; S. C. Sours et al. 2026; D. Vassiladis 2026), provides a valuable multispacecraft constellation near L1. The magnetic-field data available through NASA's CDAWeb are obtained from IMAP's Magnetometer (MAG) (`IMAP_MAG_L2_NORM-RTN`; T. S. Horbury et al. 2026), Wind's Magnetic Field Investigation (MFI) (`WI_H3-RTN_MFI`; A. Koval et al. 2023), ACE/MAG (`AC_H3_MFI`; C. Smith & N. Ness 2022), and DSCOVR/MAG (`DSCOVR_H0_MAG`; A. Koval 2026). The SOLAR-1 magnetic-field data available through NOAA/SWPC are obtained from SOLAR-1/MAG (`mag-l3_solar1`; R. Torbert et al. 2026). The solar-wind proton data used in this study are obtained from IMAP/SWAPI (`IMAP_SWAPI_L3A_PROTON-SW`; J. S. Rankin et al. 2025) and Wind's Three-Dimensional Plasma and Energetic Particle Investigation (3DP) (`WI_PM_3DP`; R. P. Lin et al. 2021a). Energetic-particle measurements are obtained from IMAP/CoDICE-Hi, including the omnidirectional intensity (`IMAP_CODICE_L2_HI-OMNI`) and pitch-angle-dependent intensity (`IMAP_CODICE_L3B_HI-PITCH-ANGLE`; S. A. Livi et al. 2025), and from IMAP's High-energy Ion Telescope (HIT) (`IMAP_HIT_L2_STANDARD-INTENSITY`; E. R. Christian et al. 2026). Wind

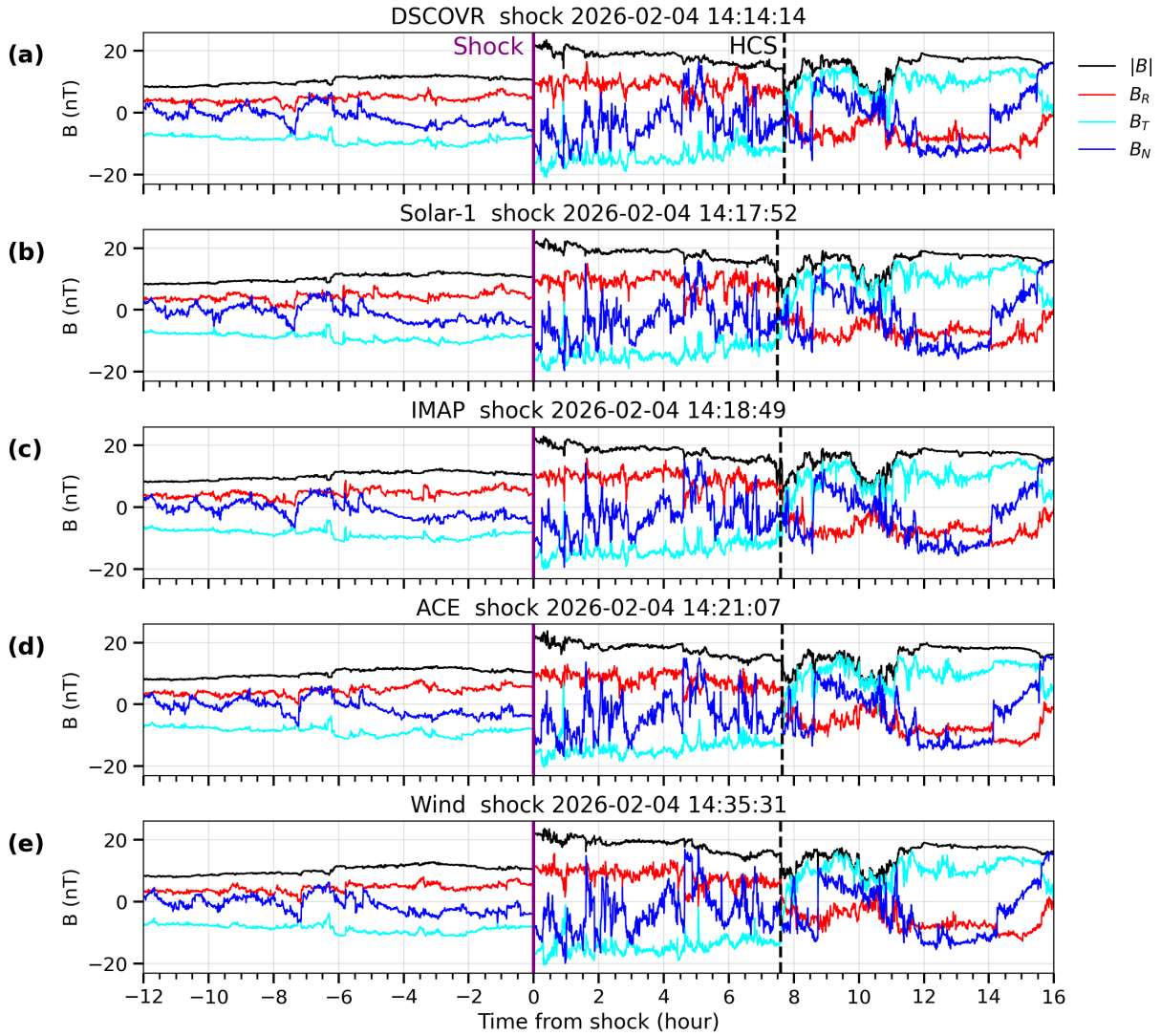


Figure 1. Magnetic-field magnitude and components measured by DSCOVR, SOLAR-1, IMAP, ACE, and Wind at a cadence of 16 s, spanning 12 hr upstream to 16 hr downstream of the shock. For each spacecraft, the time axis is referenced to its respective shock-crossing time, with $t = 0$ marking the shock arrival.

energetic-ion data are obtained from the 3DP Solid Space Telescope (SST) Open instrument, using `WI_SOSP_3DP` (R. P. Lin et al. 2021b) for omnidirectional intensity and `WI_SOPD_3DP` (R. P. Lin et al. 2021c) for pitch-angle-dependent intensity. ACE energetic-ion measurements are obtained from ACE/EPAM (`AC_H3_EPM`; R. E. Gold et al. 2022). The suprathermal-electron PADs are obtained from IMAP's Solar Wind Electron (SWE) instrument (`IMAP_SWE_L3_SCI`; R. M. Skoug et al. 2026) and Wind/3DP (`WI_ELPD_3DP`; R. P. Lin et al. 2021d).

Figure 1 shows the magnetic-field magnitude $|B|$ and components B_R, B_T, and B_N measured by DSCOVR, SOLAR-1, IMAP, ACE, and Wind from 12 hr upstream to 16 hr downstream of the shock. The shock-crossing time at each spacecraft is identified independently from the magnetic-field measurements. Since high-resolution plasma measurements in the immediate vicinity of the shock are not available for all spacecraft, and Wind lacks plasma data for about 6 minutes upstream of the shock, the local shock-arrival times are determined from the magnetic-field discontinuities. The magnetic-field time series is then shifted relative to the respective shock-crossing time, such that $t = 0$ (purple vertical line) marks the local shock arrival. Despite their spatial separation and different shock-arrival times, all spacecraft show a similar large-scale magnetic-field evolution, with a relatively quiet upstream region followed by enhanced field strength and stronger fluctuations downstream of the shock. A prominent radial magnetic-field B_R reversal occurs approximately 7.7 hr after the shock. The reversal is accompanied by a decrease in $|B|$ to near zero, indicating a possible HCS crossing (vertical dashed line). The crossing is examined in more detail below. At later times, ∼12–16 hr after the shock, the spacecraft encounter a large-scale magnetic cloud (MC), which is identified in more detail below based on its associated plasma signatures. In this study, we focus primarily on the sheath region between the shock and the ejecta, with the HCS/HPS located near the trailing edge of the sheath. As shown in Figure 1, this region is characterized by enhanced magnetic-field fluctuations and multiple current-sheet-like structures.

Figure 2(a) shows the spacecraft configuration in the L1 region near the shock-crossing time. For each spacecraft, the position is evaluated at its respective shock-crossing time. The five spacecraft are located at different positions around L1,

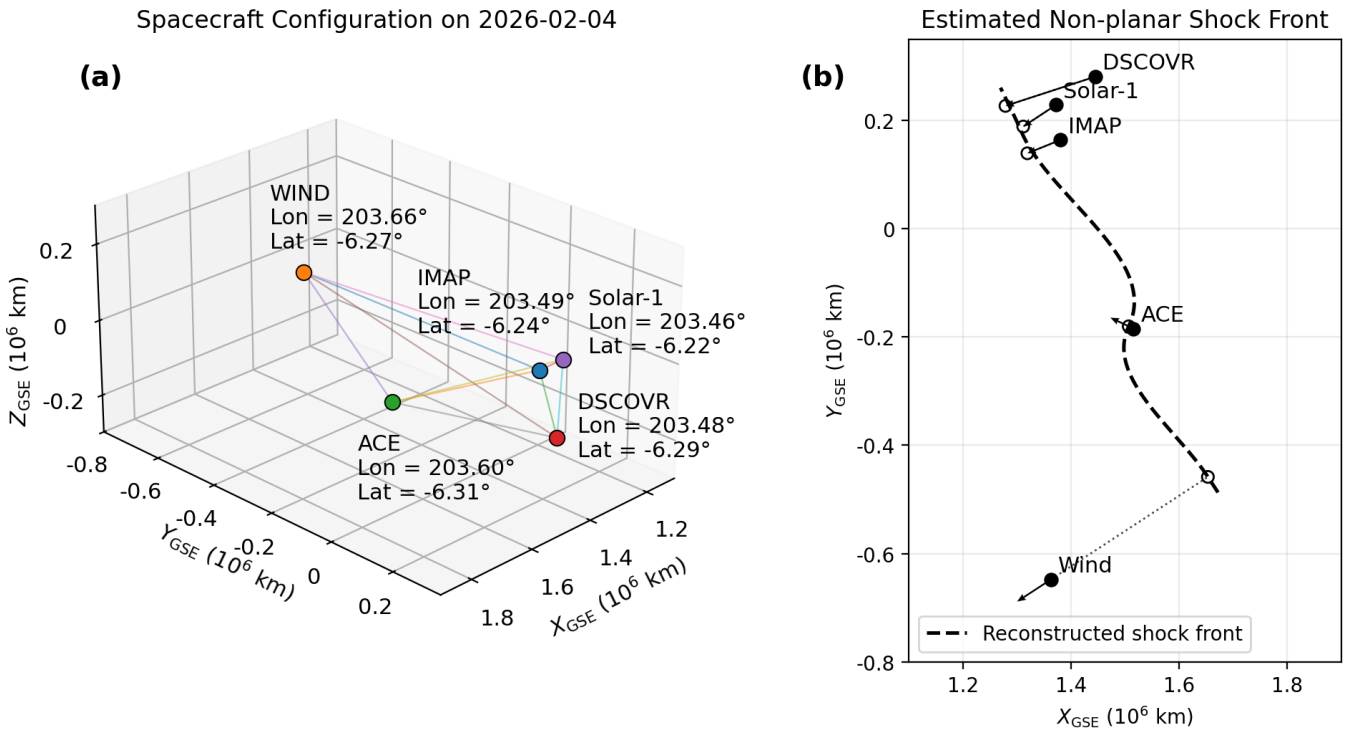


Figure 2. Multispacecraft configuration and estimated nonplanar shock front near L1. Left: positions of IMAP, Wind, ACE, DSCOVR, and SOLAR-1 in GSE coordinates near the shock crossing. Right: estimated nonplanar shock front in the GSE X–Y plane at the reference time 2026 February 4 14:21:42 UT. The filled circles mark the spacecraft positions at their respective shock-crossing times, while the open circles indicate the corresponding shock locations propagated to the reference time. The arrows show the local shock-normal directions, and the black dashed curve represents the estimated nonplanar shock front.

providing spatially separated observations of the same IP shock. For the multispacecraft timing analysis, we adopt a first-order approximation in which the shock front is assumed to be planar across the spatial extent of the spacecraft constellation, neglecting curvature and higher-order spatial variations, and to propagate at an approximately constant speed during the spacecraft crossings. Under this approximation, the difference in shock-arrival time between two spacecraft satisfies

$$V_{\rm shock}\Delta t_{ij} = \Delta \boldsymbol{r}_{ij} \cdot \hat{\boldsymbol{n}}, \tag{1}$$

where $\Delta t_{ij} = t_i - t_j$ is the difference in shock-arrival time and $\Delta \boldsymbol{r}_{ij} = \boldsymbol{r}_i(t_i) - \boldsymbol{r}_j(t_j)$ is the corresponding spacecraft separation. Here, $\hat{\boldsymbol{n}}$ is the shock normal and $V_{\rm shock}$ is the shock-propagation speed along the normal in the spacecraft frame. Defining $\boldsymbol{m} = \hat{\boldsymbol{n}}/V_{\rm shock}$, the timing relations can be written as $\Delta \boldsymbol{r}_{ij} \cdot \boldsymbol{m} = \Delta t_{ij}$. With five spacecraft, four independent timing relations are available for the three components of $\boldsymbol{m}$, and the system is solved using a least-squares method. The shock normal and propagation speed are then obtained from $\hat{\boldsymbol{n}} = \boldsymbol{m}/|\boldsymbol{m}|$ and $V_{\rm shock} = 1/|\boldsymbol{m}|$, respectively. The multispacecraft timing analysis (C. T. Russell et al. 1983; G. Paschmann & P. W. Daly 1998) yields a shock normal of $\hat{\boldsymbol{n}} = (-0.85, -0.52, 0.04)$ in GSE coordinates and a propagation speed of $V_{\rm shock} = 437\,{\rm km\,s^{-1}}$ along the shock normal in the spacecraft frame. To estimate the uncertainties in the multispacecraft timing solution, we assume a Gaussian uncertainty with a standard deviation of 5 s for the shock-arrival time at each spacecraft. The value $\sigma_t = 5$ s is adopted as a conservative estimate of the uncertainty in identifying the magnetic-field discontinuity associated with the shock crossing. For each Monte Carlo realization, an independent random timing perturbation is drawn from the assumed Gaussian distribution for each of the five spacecraft. The resulting perturbed shock-arrival times are then simultaneously fitted using the same least-squares procedure, and the corresponding $\hat{\boldsymbol{n}}$ and $V_{\rm shock}$ are recalculated. This procedure is repeated for 10^5 Monte Carlo realizations while keeping the spacecraft positions fixed. The uncertainties in the components of $\hat{\boldsymbol{n}}$ and $V_{\rm shock}$ are taken as the standard deviations of the corresponding Monte Carlo distributions. These uncertainties quantify the effect of the assumed-shock-arrival-time uncertainty and do not account for systematic uncertainties associated with the planar-front approximation or shock-front curvature.

To characterize the local shock geometry at each spacecraft and provide directional constraints for the shock-front estimation, we independently determine the local shock normal using the magnetic coplanarity method (D. S. Colburn & C. P. Sonett 1966; K. Moreland et al. 2023). To reduce the sensitivity of the derived normal to the selection of upstream and downstream averaging intervals, we adopt a statistical averaging procedure similar to that implemented in SerPyShock (D. Trotta et al. 2022). The upstream and downstream averaging-window lengths are varied independently from 2 to 6 minutes in 30 s increments, resulting in $N = 81$ window pairs, while their inner boundaries are fixed at 30 s before and after the shock, respectively, to exclude the shock transition. For each combination of upstream and downstream averaging windows, the mean magnetic fields $\boldsymbol{B}_1$ and $\boldsymbol{B}_2$ and their component-wise standard deviations are calculated. We then generate 10^5 Monte

Table 1
Shock-normal Components (n_x, n_y, n_z) in GSE Coordinates, Shock Obliquity θ_{Bn}, Magnetic-field-compression Ratio B_2/B_1, and Shock-propagation Speed

Spacecraft	Arrival Time (UT)	n_x	n_y	n_z	θ_{Bn} (deg)	B_2/B_1	V_{sh} (km s^{-1})
DSCOVR	14:14:14	-0.88 ± 0.39	-0.27 ± 0.26	0.39 ± 0.20	84.0 ± 2.7	2.05 ± 0.05	⋯
SOLAR-1	14:17:52	-0.82 ± 0.14	-0.57 ± 0.15	0.02 ± 0.29	83.0 ± 2.2	2.06 ± 0.04	⋯
IMAP	14:18:49	-0.83 ± 0.19	-0.36 ± 0.30	0.42 ± 0.40	83.4 ± 2.7	2.10 ± 0.06	⋯
ACE	14:21:07	-0.64 ± 0.21	0.28 ± 0.23	0.72 ± 0.16	74.8 ± 5.3	2.06 ± 0.09	⋯
Wind	14:35:31	-0.83 ± 0.29	-0.55 ± 0.22	-0.10 ± 0.51	86.3 ± 1.7	2.08 ± 0.04	⋯
Multispacecraft	⋯	-0.85 ± 0.02	-0.52 ± 0.02	0.04 ± 0.04	⋯	⋯	437 ± 18

Carlo realizations of $\boldsymbol{B}_1$ and $\boldsymbol{B}_2$ by Gaussian sampling of each magnetic-field component and calculate the corresponding shock normal $\hat{\boldsymbol{n}}$, shock obliquity θ_{Bn}, and magnetic-field-compression ratio B_2/B_1. For each of these derived quantities, the jth window pair yields a mean μ_j and standard deviation σ_j. The final estimate for each quantity is taken as the average of the means over all window pairs, $\bar{\mu} = \frac{1}{N}\sum_{j=1}^{N}\mu_j$, and its uncertainty is estimated as $\sigma_{\rm final} = \left[\frac{1}{N}\sum_{j=1}^{N}(\sigma_j^2 + (\mu_j - \bar{\mu})^2)\right]^{1/2}$. This uncertainty accounts for both the Monte Carlo variability within individual window pairs and the sensitivity to the choice of averaging interval. The resulting shock parameters and uncertainties are summarized in Table 1.

The magnetic coplanarity estimates show some sensitivity to the choice of averaging intervals, particularly because the downstream magnetic field exhibits strong fluctuations, as shown in Figure 1. To assess this sensitivity, we repeated the analysis using fixed shorter averaging windows of 1 and 2 minutes on both sides of the shock (L. Yang et al. 2018, 2019; Z. Liu et al. 2022; X. Guo et al. 2026). The resulting θ_{Bn} and B_2/B_1 values are consistent, within uncertainties, with those obtained from the 2 to 6 minute window ensemble, and the quasiperpendicular classification remains unchanged at all five spacecraft.

Table 1 shows that the shock normal obtained from the multispacecraft timing analysis differs from the local coplanarity estimates by about 5° at Wind, 2° at SOLAR-1, and about 20° at IMAP and DSCOVR, with a substantially larger deviation at ACE. Given the uncertainties in the local normal estimates, part of these differences may reflect limitations of the coplanarity method. For highly quasiperpendicular shocks, the upstream and downstream magnetic-field directions can be very similar, such that $|\boldsymbol{B}_1 \times \boldsymbol{B}_2|$ becomes small, making the magnetic coplanarity normal sensitive to relatively small changes in the field direction. Some contribution from spatial variations of the shock front across the L1 constellation cannot be excluded (S. Raptis et al. 2026). Nevertheless, the derived θ_{Bn} values consistently indicate a quasiperpendicular shock across the L1 constellation.

The local shock normals listed in Table 1 are then used to constrain the nonplanar shock front shown in Figure 2(b). Following the approach of M. Neugebauer & J. Giacalone (2005), each shock crossing is propagated from the spacecraft position (filled circles) to a reference time along the local shock normal. The reference time, 14:21:42 UT, is taken to be the mean of the five shock-crossing times. Because local plasma measurements near the shock are not available at every spacecraft, we use the shock speed obtained from the multispacecraft timing analysis for all locations. The propagated positions (open circles) therefore provide spatial constraints on the shock front at the reference time. A smooth representation of the front is constructed by connecting the propagated positions with cubic Bézier segments. The tangent at each constraint point is chosen to be perpendicular to the corresponding local shock normal. For closely spaced spacecraft (e.g., DSCOVR, SOLAR-1, and IMAP), neighboring propagated positions and shock normals are pairwise averaged before constructing the cubic Bézier segments. Therefore, the reconstructed shock front is based on these averaged constraints and is not required to pass exactly through every individual open-circle center. The resulting black dashed curve represents an approximate reconstruction of the curved shock front. The reconstructed shock front shows departures from the first-order planar approximation, with a characteristic radius of curvature of order $\sim 10^6$ km. This value is consistent with previous multispacecraft observations of IP shocks near 1 au, for which local radii of curvature were found to range from approximately 3×10^5 to 10^7 km, with a mean of a few 10^6 km (M. Neugebauer & J. Giacalone 2005). These curvature lengths are also comparable to the correlation length of magnetic-field fluctuations near 1 au (W. Matthaeus et al. 2005), suggesting that large-scale magnetic fluctuations in the solar wind may contribute to distortions of the shock front.

3. Energetic-ion Enhancement Associated with the 2026 February 4 Shock

Figure 3 presents an overview of IMAP in situ measurements of energetic protons, the magnetic field, and solar-wind plasma associated with the 2026 February 4 shock. The magnetic-field magnitude and vector components in RTN coordinates shown in Figure 3(c) are provided by IMAP/MAG at a cadence of 2 Hz. The solar-wind proton data in Figures 3(g)–(h) are obtained from IMAP/SWAPI at a cadence of 1 minute. The omnidirectional energetic-proton differential intensities in Figure 3(a) are obtained from IMAP/HIT over ∼3–5.5 MeV, while those in Figure 3(b) are obtained from IMAP/CoDICE-Hi over ∼0.1–2 MeV. The 270 eV suprathermal-electron PAD in Figure 3(d) is obtained from IMAP/SWE.

The magnetic-field orientation is further illustrated by the elevation angle θ_B, which measures the north–south tilt of the field relative to the RT plane, and the azimuthal angle ϕ_B, which describes the field direction within the RT plane. The shock crossing is indicated by the solid vertical line. As discussed above, the shock is quasiperpendicular and has a magnetic-compression ratio of about 2. The HCS crossing is identified at about 22:00 UT on 2026 February 4 by the magnetic-field-polarity reversal together with a corresponding reversal of the suprathermal-electron-strahl direction, evident in the PAD shown in Figure 3(d) (J. T. Gosling et al.

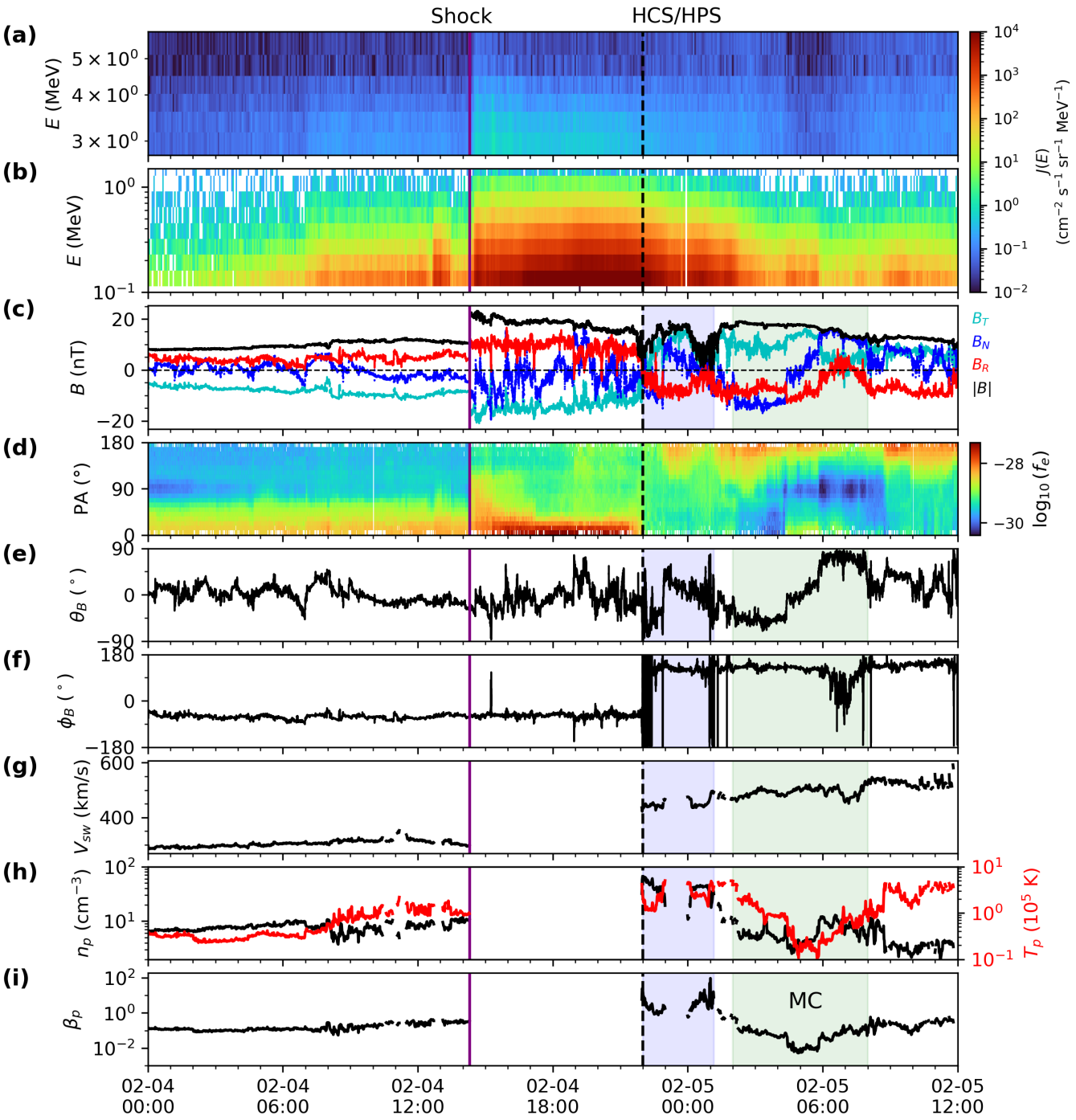


Figure 3. Overview of the 2026 February 4 shock event observed by IMAP. From top to bottom: (a) energetic-proton differential intensity from IMAP/HIT over ∼3–5.5 MeV, (b) energetic-proton differential intensity from IMAP/CODICE-Hi over ∼0.1–2 MeV, (c) magnetic-field magnitude and RTN components, (d) pitch-angle distribution of 270 eV electrons, (e) magnetic-field elevation angle θ_B, (f) magnetic-field azimuthal angle ϕ_B, (g) solar-wind speed $V_{\rm sw}$, (h) proton density n_p and temperature T_p, and (i) proton plasma beta β_p. The solid vertical line marks the shock crossing, and the dashed vertical line marks the HCS crossing. The purple-shaded interval denotes the HCS/HPS region, while the green-shaded interval marks the magnetic cloud (MC) associated with the ejecta driving the shock.

2005b, 2006). The HCS crossing occurs within the highly disturbed downstream sheath region. The enhanced proton plasma beta surrounding the HCS, accompanied by increased plasma density, indicates that the HCS is embedded within a broader heliospheric plasma sheet (HPS; D. Winterhalter et al. 1994; N. Crooker et al. 2004). The extent of the HPS (purple-shaded interval) is better constrained by the Wind observations discussed below because of their continuous plasma coverage. The strongly varying magnetic-field azimuthal angle ϕ_B within the HPS further reflects the disturbed magnetic-field configuration. Following the HCS/HPS interval, an MC associated with the IP ejecta driving the shock is observed. The MC, indicated by the green shading, is characterized by an enhanced magnetic-field magnitude, smooth field rotation, reduced proton temperature, and very low plasma beta (e.g., L. Klein & L. Burlaga 1982; L. Burlaga et al. 1990).

The several-MeV proton intensities in Figure 3(a) show little enhancement upstream of the shock. In contrast, the sub-MeV proton intensities in Figure 3(b) begin increasing well upstream, with a more pronounced rise developing around 07:00 UT on February 4. The relatively weak response at several MeV may partly reflect the modest shock strength, with a compression ratio of about 2, as shown in Table 1. Across the shock, energetic-proton intensities increase at all measured energies. Farther downstream, however, the evolution becomes energy dependent. Below ∼1 MeV, proton intensities remain strongly enhanced for several hours until the HCS/HPS crossing. In contrast, intensities above ∼1 MeV show much weaker downstream variations and tend to peak closer to the shock. Following the HCS/HPS crossing, energetic-proton intensities show an overall decrease, although localized enhancements remain evident at lower energies. A pronounced reduction in the several-MeV intensities is observed after entry into the MC, possibly reflecting changes in magnetic connectivity and particle transport. The energy-dependent evolution throughout the downstream sheath suggests that the low-energy proton population is influenced by downstream processes in addition to the shock.

Figure 4 presents the Wind observations of the same event. Omnidirectional energetic-ion intensities from approximately 0.2 to 4.4 MeV, with a cadence of about 12 s, are obtained from Wind/3DP/SOSP. Figure 4(a) shows the energy–time spectrogram of the differential intensity, while Figure 4(b) shows the corresponding time–intensity profiles at selected energies between 0.20 and 4.44 MeV, averaged over 5 minute intervals. The Wind measurements show the same overall energy-dependent behavior observed by IMAP. The upstream enhancement is relatively weak, particularly at higher energies. Across the shock, intensities increase in all measured channels, but the subsequent downstream evolution varies with energy. Sub-MeV intensities remain elevated through much of the downstream region, whereas the >2 MeV ion intensities in Figure 4(b) show no clear downstream enhancement and gradually decrease farther downstream of the shock, consistent with the IMAP observations shown in Figures 3(a) and (b).

Approximately 6 hr upstream of the shock, around 08:00 UT on February 4, the solar wind encounters a distinct magnetic structure characterized by a gradual increase in $|B|$ and a smooth rotation of B_N, also reflected in the variation of θ_B. The magnetic-field enhancement is accompanied by a decrease in proton density n_p and an increase in proton temperature T_p. A similar structure is also evident in the IMAP observations shown in Figure 3. The sub-MeV proton intensities show a noticeable abrupt increase near the boundary of this structure.

Downstream of the shock, the magnetic-field direction becomes substantially more variable. As shown in Figures 4(e) and (f), both the elevation angle θ_B and azimuthal angle ϕ_B undergo pronounced variations throughout the sheath, indicating substantial changes in the local magnetic-field orientation and the presence of current-sheet-like structures. Around 19:00 UT on February 4, both θ_B and ϕ_B show noticeable directional changes. At approximately the same time, the suprathermal-electron PAD in Figure 4(d), obtained from Wind/3DP, remains dominated by parallel streaming, while the distribution broadens and the antiparallel flux near 180° becomes enhanced, suggesting a possible change in magnetic connectivity. A similar evolution is also evident in the IMAP observations shown in Figures 3(d)–(f). The lowest-energy ion intensity (0.20 MeV) also reaches a broad downstream maximum around this interval, about 3 times the intensity measured immediately downstream of the shock. These coincident changes suggest that variations in magnetic connectivity within the structured downstream sheath may contribute to the redistribution of energetic particles.

Similar to the IMAP observations, Wind encounters the HCS about 7.7 hr after the shock, at approximately 22:18 UT on February 4. The HCS is identified by the magnetic-field-polarity reversal, while the surrounding interval of enhanced proton plasma beta, reaching values of about 10^2, is identified as the broader HPS, extending until approximately 01:30 UT on February 5 (purple-shaded region). Within the HPS, $|B|$ exhibits localized enhancements, as shown in Figure 4(c), suggesting the presence of compressed magnetic structures embedded within the disturbed plasma sheet. Such magnetic compression may contribute to localized particle energization through adiabatic compression. The broader HPS also contains multiple secondary current sheets, one of which is observed near 23:20 UT on February 4 and is examined in more detail below. Following the HCS/HPS, Wind enters the large-scale MC. Although not the focus of this study, the energetic-ion intensities show an overall decrease within the MC, particularly at higher energies such as 4.4 MeV, as shown in Figure 4(b).

Figure 5 compares omnidirectional energetic-ion time–intensity profiles observed by IMAP/CoDICE-Hi (Figure 5(a)), Wind/3DP/SOSP (Figure 5(c)), and ACE/EPAM (Figure 5(e)) over a 36 hr interval centered on their respective shock crossings. Because the measurements are obtained using different detector techniques and species-selection capabilities, some cross-instrument differences are expected. IMAP/CoDICE-Hi provides species-resolved intensities, whereas the Wind/3DP SST Open measurements are proton-calibrated but have limited species discrimination, so heavier ions may contribute to the reported proton intensities. Similarly, the ACE/EPAM LEMS30 and LEMS120 telescopes measure ions without unambiguous species separation. Absolute intensities should consequently be compared with caution, while the overall temporal and energy-dependent trends are considered more robust. For ACE, we use the 0.068–4.8 MeV omnidirectional ion intensities obtained by averaging measurements from the EPAM LEMS30 and LEMS120 telescopes. For consistency, all time–intensity profiles shown in Figure 5 are averaged over 5 minute intervals.

Despite these instrumental differences, all three spacecraft observe an extended enhancement of sub-MeV ions downstream of the shock. The lowest-energy intensities reach a broad maximum about 5 hr downstream, at levels approximately 3 times higher than those observed immediately downstream of the shock. In contrast, intensities above ∼1 MeV show a much weaker downstream enhancement and reach their maximum near the shock. The broadly consistent timing and energy dependence across the three spacecraft indicate that the extended downstream sub-MeV ion enhancement is not confined to a single spacecraft location, but extends across the region sampled by the L1 constellation.

The contrasting downstream evolution at low and high energies is consistent with energy-dependent particle transport. Higher-energy ions generally have larger diffusion coefficients and can diffuse away from the shock and through the downstream sheath more efficiently, whereas lower-energy ions remain more strongly scattered and can persist longer within the disturbed sheath region. Changes in magnetic connectivity to different portions of a structured shock surface

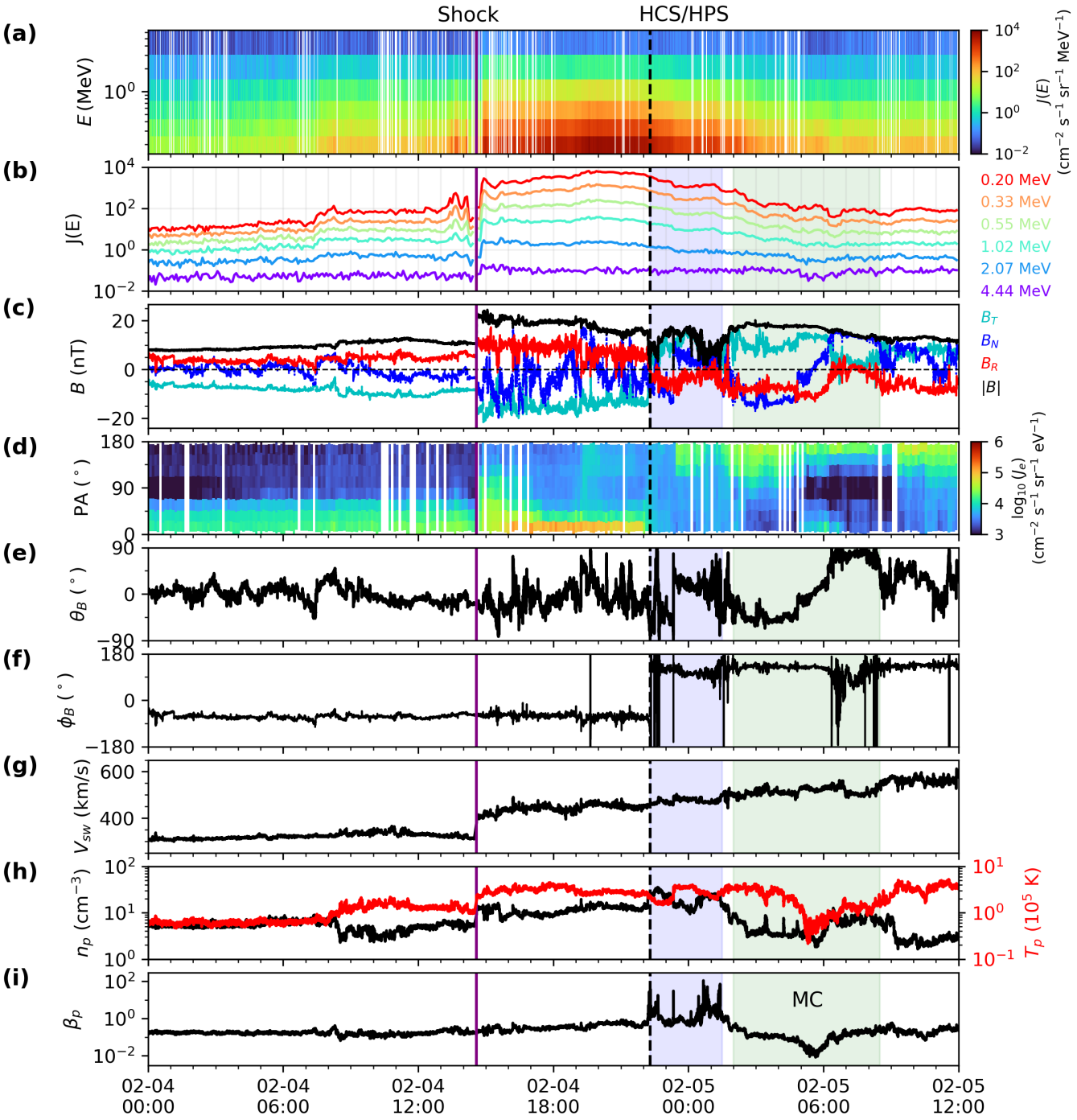


Figure 4. Same as Figure 3, but for Wind observations. (a) The energy–time spectrogram of energetic-ion differential intensity from Wind/3DP/SOSP measurements and (b) the corresponding 5 minute averaged time–intensity profiles at selected energies from 0.20 to 4.44 MeV. (c)–(i) The magnetic field, 290 eV electron pitch-angle distribution from Wind/3DP, magnetic-field orientation, solar-wind-plasma parameters, and proton plasma beta in the same format as Figure 3. The solid vertical line marks the shock crossing, the dashed vertical line marks the HCS crossing, and the purple- and green-shaded intervals denote the HCS/HPS and magnetic cloud, respectively.

can further redistribute energetic particles and displace the low-energy intensity maximum from the local shock crossing (J. Giacalone & M. Neugebauer 2008; M.-Y. Lo et al. 2026). Additional localized energization within the downstream sheath region, particularly near the disturbed HCS/HPS, cannot be excluded. Such processes may include interactions with reconnecting current sheets and other small-scale current-sheet-like structures, which can provide localized particle energization, scattering, and trapping (J. F. Drake et al. 2006; G. P. Zank et al. 2015; J. A. le Roux et al. 2016; H. Hakobyan et al. 2021). These processes may be particularly effective for the lower-energy ion population (e.g., M. I. Desai et al. 2025), for which modest energy gains can produce a more pronounced intensity enhancement.

The first-order anisotropy A_1 is calculated from the pitch-angle-dependent intensities of 0.16–0.32 MeV protons from

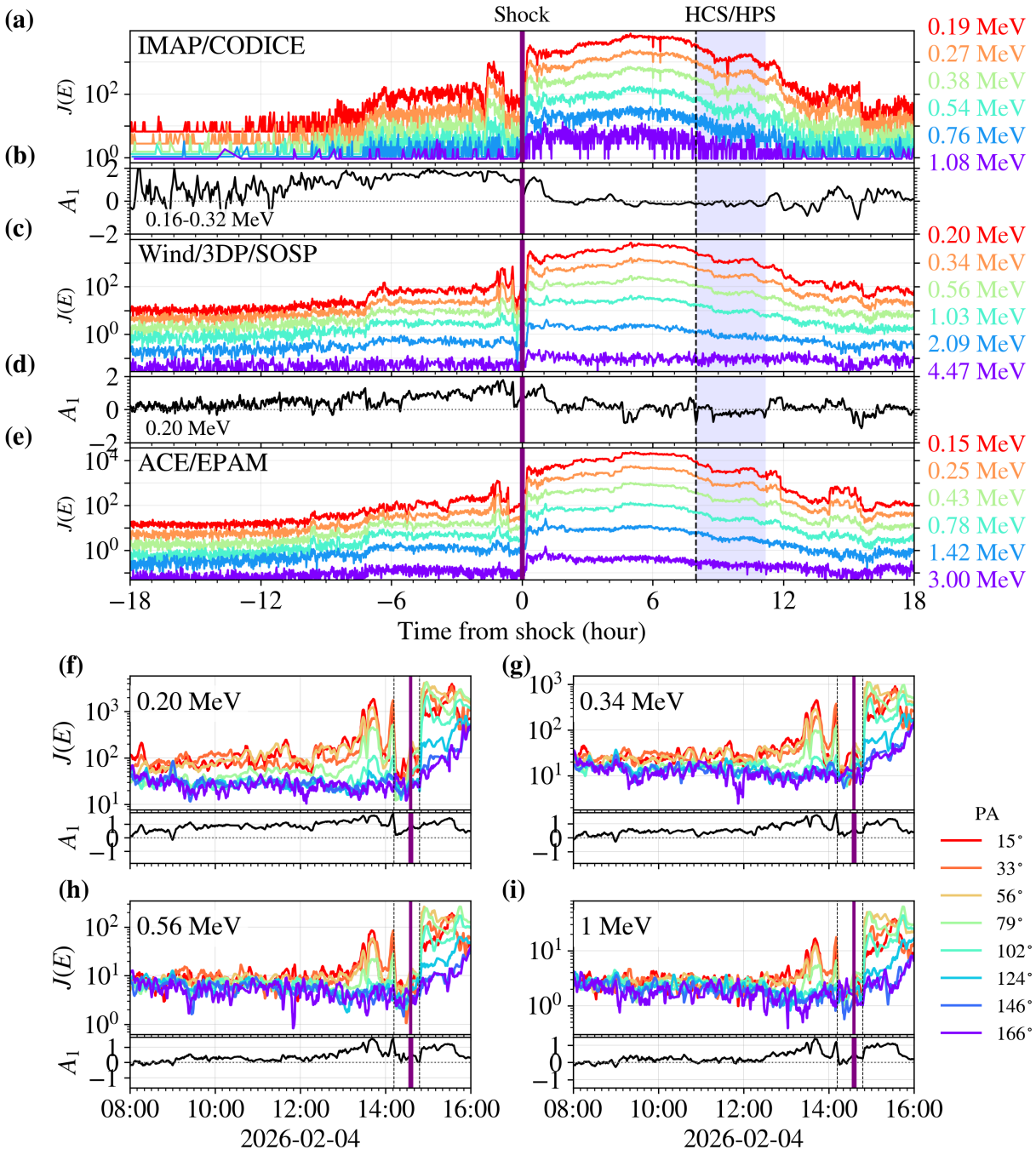


Figure 5. Multispacecraft energetic-ion observations across the 2026 February 4 IP shock. (a), (c), and (e) Omnidirectional intensities from IMAP/CoDICE-Hi, Wind/3DP/SOSP, and ACE/EPAM, respectively. (b) and (d) The first-order anisotropy A_1 near 0.2 MeV, calculated from pitch-angle-dependent intensities measured by IMAP/CoDICE-Hi and Wind/3DP/SOPD, respectively. (f)–(i) An expanded view of the Wind/3DP/SOPD observations around the shock crossing at 0.20, 0.34, 0.56, and 1 MeV, respectively, including pitch-angle-dependent intensities and the corresponding A_1. The solid purple line marks the shock crossing.

IMAP in Figure 5(b) and 0.20 MeV from Wind in Figure 5(d). Following N. Dresing et al. (2014), the first-order anisotropy is calculated as

$$A_1 = 3\frac{\int_{-1}^{1} J(\mu)\mu d\mu}{\int_{-1}^{1} J(\mu) d\mu}, \quad (2)$$

where μ is the pitch-angle cosine and $J(\mu)$ is the pitch-angle-dependent particle intensity. The sign of A_1 indicates the net streaming direction, with $A_1 > 0$ corresponding to parallel streaming, $A_1 < 0$ to antiparallel streaming, and $A_1 \approx 0$ indicating little net field-aligned anisotropy. Pronounced anisotropy is observed upstream of the shock at both IMAP and Wind, indicating field-aligned streaming of low-energy ions as the shock approaches. Downstream of the shock, A_1 becomes appreciable within ~10 minutes of the crossing and remains so for about one hour, indicating that a strong streaming component persists shortly after shock passage. Farther downstream, A_1 decreases toward values close to zero even though the sub-MeV proton intensities remain strongly

enhanced. This reduction in net streaming is consistent with increased pitch-angle scattering. However, $A_1 \approx 0$ does not necessarily imply an isotropic distribution, because a PAD symmetric about 90°, such as a pancake-like distribution, also has a vanishing A_1. The detailed pitch-angle evolution is examined in Section 4.

We also note a short-lived reduction in low-energy ion intensities observed by all three spacecraft within about 15 minutes of their respective shock crossings, extending slightly downstream. Figures 5(f)–(i) show the Wind/3DP/SOPD energetic-ion intensities at eight pitch angles for 0.20, 0.34, 0.56, and 1.0 MeV, respectively. Here, pitch angle is defined relative to the local magnetic-field direction, such that 0° and 180° correspond to particles moving parallel and antiparallel to $\boldsymbol{B}$, respectively. The two vertical dotted lines in Figures 5(f)–(i) mark the interval associated with this near-shock intensity decrease. The reduction is most pronounced in the pitch-angle channels that are enhanced farther upstream, particularly at small pitch angles. As this field-aligned component weakens, the PAD broadens and A_1 approaches zero within the interval bounded by the two dotted lines. The pronounced upstream field-aligned population, especially at low energies, is consistent with ions streaming along magnetic field lines connected to the shock. The short-lived near-shock intensity decrease is primarily associated with the disappearance of this field-aligned component, whereas the other pitch-angle channels show comparatively smaller changes, as shown in Figures 5(f)–(i). We do not identify a distinct magnetic-field feature during this short interval that provides independent evidence for a change in magnetic connectivity. The disappearance of the field-aligned component may instead be related to the highly quasiperpendicular shock geometry, for which field-aligned particle motion has only a small component normal to the shock surface, potentially affecting the transport of the upstream field-aligned population across the shock. Spatial and/or temporal variations in particle acceleration at the shock may also contribute to the short-lived intensity decrease, although their relative importance cannot be determined from the present observations.

The first-order anisotropy A_1 also shows a clear energy dependence. Upstream, A_1 remains positive and relatively large at 0.20 MeV as shown in Figure 5(f), whereas it is much closer to zero at 1 MeV shown in Figure 5(i). This is consistent with energy-dependent transport, i.e., lower-energy ions remain more strongly tied to the magnetic field and can exhibit pronounced field-aligned streaming along connected field lines, whereas higher-energy ions diffuse more broadly and show weaker net field-aligned anisotropy.

4. Evolution of Pitch-angle Distributions and Energy Spectra

Figure 6 examines the evolution of energetic-ion PADs observed by Wind/SOPD at a cadence of ∼12 s across the shock and downstream toward the HCS/HPS. Figures 6(a)–(d) show the time-dependent PADs for four energy channels spanning 0.34–2.09 MeV, while Figures 6(e)–(j) show PADs averaged over six representative time intervals at 0.34 MeV (red dots), 0.56 MeV (cyan dots), and 1.03 MeV (purple dots). The shock was crossed at 14:35:31 UT on February 4. Specifically, Figure 6(e) corresponds to the upstream interval from 10:00 to 12:00 UT, Figure 6(f) to an interval about one hour upstream of the shock when strong field-aligned streaming develops, Figure 6(g) to an interval beginning about 10 minutes downstream of the shock, Figure 6(h) to the downstream interval of maximum low-energy ion intensity, Figure 6(i) to the HCS/HPS interval, and Figure 6(j) to the MC interval. Each selected interval in Figures 6(e)–(j) spans 2 hr, except for Figures 6(f) and (g), for which shorter intervals are used to exclude the near-shock intensity-decrease period shown and discussed in Figure 5.

A clear energy-dependent intensity evolution is evident in Figures 6(a)–(d). At lower energies, the ion intensities reach their largest downstream values around 19:00 UT on February 4. The 2.09 MeV population in Figure 6(d) is enhanced primarily near the shock. Far upstream, the PADs are nearly isotropic at higher energies and weakly anisotropic at lower energies, as shown in Figure 6(e) and also in Figure 5. As the shock approaches, pronounced field-aligned streaming develops, as shown in Figure 6(f). This upstream field-aligned streaming is consistent with energetic particles propagating along the magnetic field from the shock into the upstream region. Within about one hour after the shock crossing, the PADs change substantially, with particle intensities becoming increasingly concentrated at oblique pitch angles, as shown in Figure 6(g). However, the distribution remains asymmetric, with intensities at PA $< 90°$ still substantially higher than those at PA $> 90°$, indicating that the field-aligned streaming component remains dominant.

Farther downstream, a distinct pancake-like PAD centered near 90° develops and persists for several hours. Similar perpendicular anisotropies downstream of IP shocks have been reported previously (e.g., L. Yang et al. 2020, 2023). The distribution gradually broadens and becomes less pronounced as the spacecraft approaches the HCS/HPS, consistent with increased pitch-angle scattering during downstream transport. Around 19:00 UT on February 4, near the maximum of the low-energy ion intensities, the PAD in Figure 6(h) becomes substantially broader and shows an enhanced antiparallel (∼180°) intensity. This change occurs near the magnetic-field directional variations discussed in Figure 4 and may reflect a temporary change in magnetic connectivity. The pancake-like anisotropy weakens after the HCS crossing and largely disappears by about 01:30 UT on February 5, near the outer edge of the HPS.

The downstream pancake-like PAD is consistent with preferential perpendicular energization. Near the shock, SDA at the quasiperpendicular shock provides one possible mechanism for producing the initial perpendicular anisotropy (e.g., R. B. Decker 1983; G. Erdös & A. Balogh 1994; I. Richardson & H. Cane 2010). Farther downstream, where direct interaction with the shock becomes less likely, local processes may contribute to maintaining or modifying the perpendicular anisotropy. For example, reconnecting current sheets and associated magnetic islands can provide sites for particle energization (J. F. Drake et al. 2009; G. P. Zank et al. 2014; J. A. le Roux et al. 2015) and, in some cases, perpendicular ion heating (A. Mallet et al. 2026). Magnetic compression provides another possible mechanism. In particular, a narrower and more pronounced enhancement centered near 90° appears within the broader HPS interval bounded by the two vertical dashed lines in Figures 6(a)–(d), coincident with an increase in $|B|$ shown in Figure 4(c). Conservation of the first adiabatic invariant during this magnetic compression can preferentially increase the perpendicular particle energy, providing a

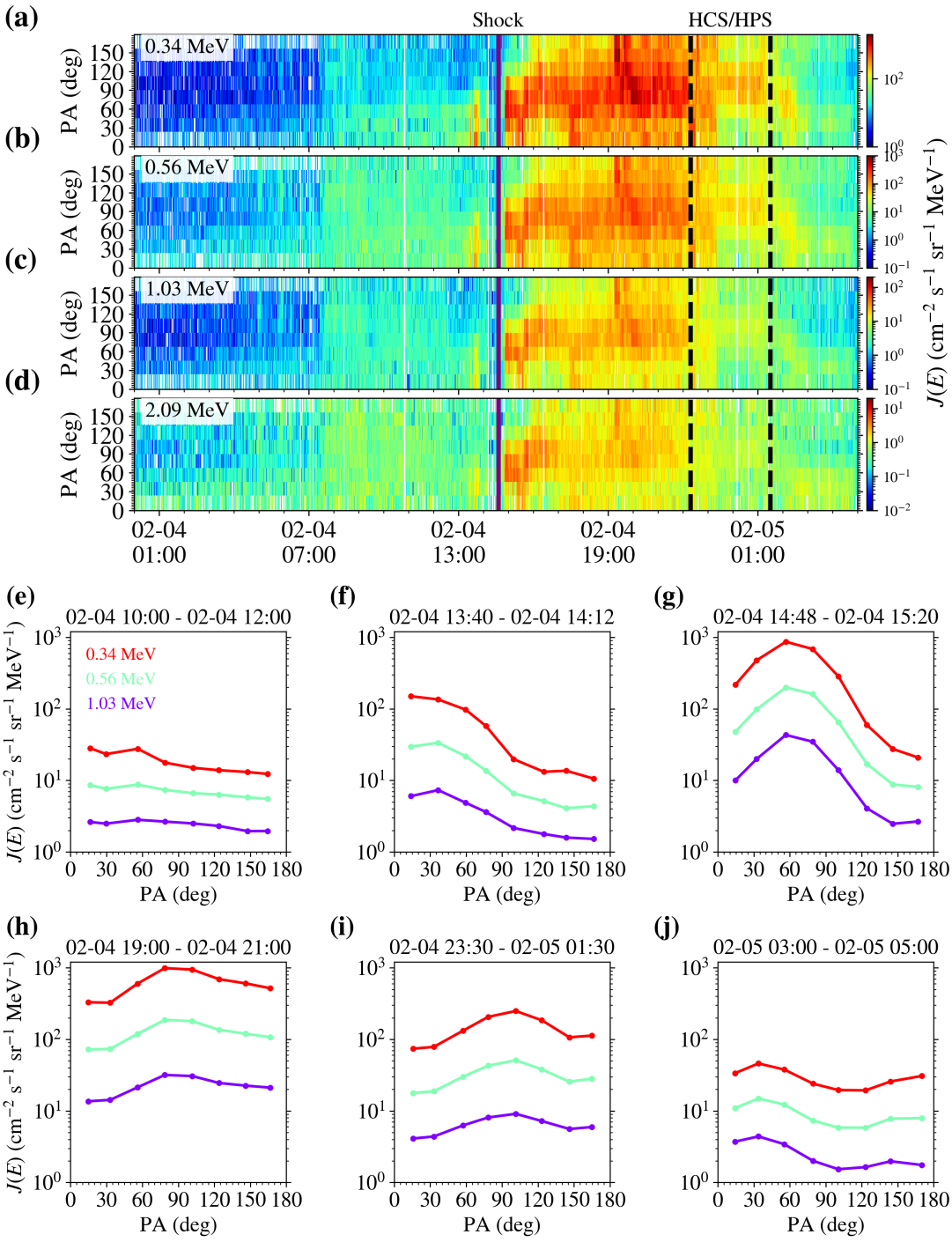


Figure 6. Evolution of energetic-ion pitch-angle distributions (PADs) observed by Wind/3DP/SOPD across the shock. (a)–(d) The time-dependent PADs for four energy channels spanning 0.34–2.09 MeV, and (e)–(j) PADs averaged over six representative intervals for 0.34 (red), 0.56 (cyan), and 1.03 (purple) MeV ions. The solid vertical line marks the shock crossing, and the region bounded by the dashed vertical lines marks the HCS/HPS interval.

possible explanation for the enhanced intensity near 90° shown in Figure 6(i).

As the spacecraft enters the following MC, the PAD in Figure 6(j) exhibits weak sunward streaming. The disappearance of the pancake-like PAD beyond the HCS/HPS may reflect changes in magnetic connectivity associated with entry into the large-scale MC. The PAD evolution examined here also clarifies the behavior of the first-order anisotropy A_1 shown in Figure 5. Although A_1 decreases toward zero farther downstream, the sub-MeV ions remain distinctly nonisotropic, with a pancake-like distribution persisting through much of the downstream sheath. IMAP/CoDICE-Hi observations show a similar evolution at a cadence of ∼4 minutes, as discussed in detail by M. A. Dayeh et al. (2026).

Figure 7 compares omnidirectional energetic-ion energy spectra measured by Wind/3DP/SOSP, ACE/EPAM, IMAP/CoDICE-Hi, and IMAP/HIT during six representative intervals spanning the quiet upstream (Figure 7(a)), preshock (Figures 7(b)–(c)), downstream (Figures 7(d)–(e)), and HCS/HPS (Figure 7(f)) periods. To facilitate comparison with

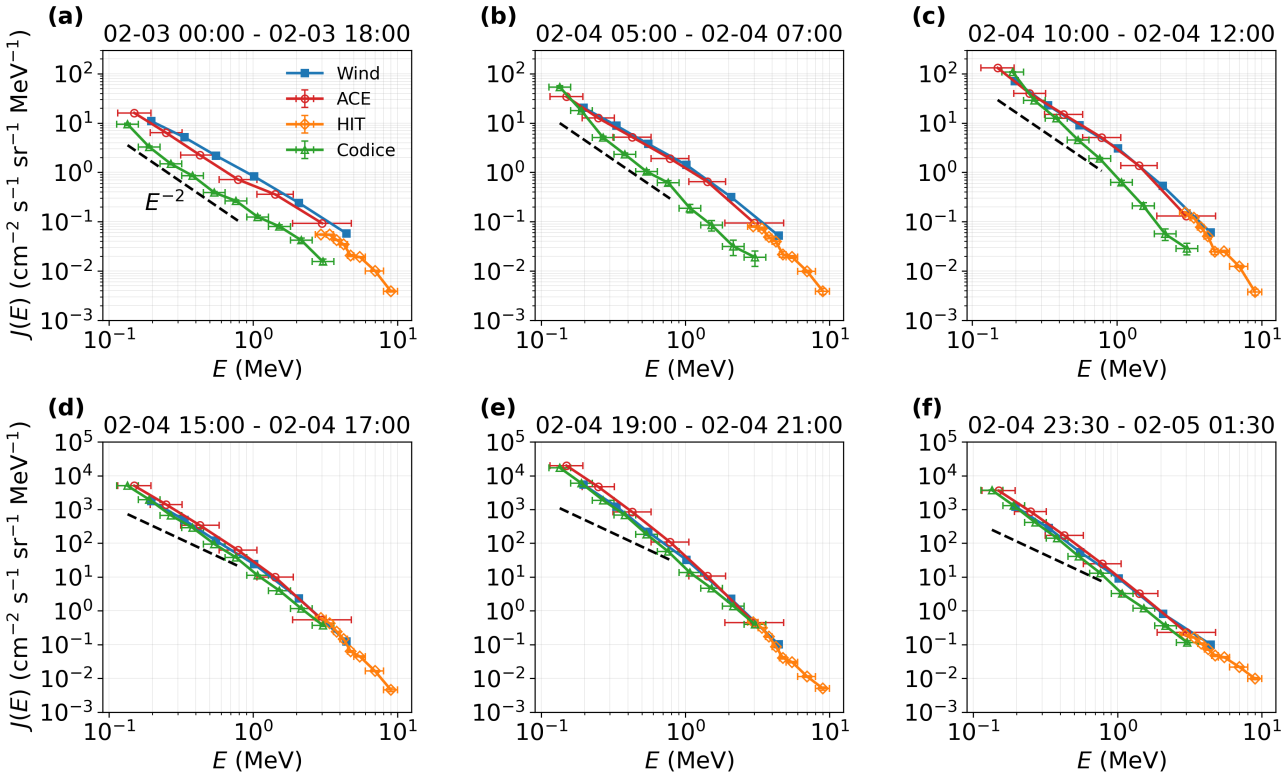


Figure 7. Energetic-ion energy spectra measured by Wind/3DP/SOSP, ACE/EPAM, IMAP/CoDICE-Hi, and IMAP/HIT during six representative intervals spanning the quiet upstream (a), preshock (b)–(c), downstream (d)–(e), and HCS/HPS (f) periods. The averaging intervals are referenced to the Wind times. The corresponding IMAP and ACE intervals are shifted according to their respective local shock-crossing times. Cross-instrument differences are largest during the low-intensity upstream intervals (a)–(c), where CoDICE-Hi counting rates approach the instrumental background level and viewing-direction effects may also be important. Dashed lines indicate an E^{-2} dependence for reference.

the energetic-ion measurements from Wind and ACE, the CoDICE-Hi spectra shown here are constructed by summing the H, ^{4}He, O, and Fe contributions. Wind/3DP and ACE/EPAM measure energetic ions with limited species discrimination, whereas CoDICE-Hi identifies individual ion species (S. A. Livi et al. 2025). The HIT proton spectrum is shown separately as a higher-energy reference, no significant heavy ions are detected by HIT during this event. The averaging intervals are referenced to the Wind observation times. For IMAP and ACE, the intervals are shifted according to their respective local shock-crossing times so that they correspond approximately to the same temporal distance from the shock. The dashed E^{-2} lines indicate the approximate test-particle DSA spectral slope expected for a compression ratio of $r \approx 2$. Because the shock is highly quasiperpendicular, we assume that the plasma compression ratio is approximately equal to the measured magnetic-field compression ratio, $r \simeq B_2/B_1$, as expected for a nearly perpendicular MHD shock. Energy and flux uncertainties are not publicly available for the Wind/3DP SOSP and SOPD data products used here. Accordingly, uncertainties in the averaged intensities are shown only for ACE and IMAP and are derived from their reported measurement uncertainties using standard error propagation.

During the quiet and early upstream intervals in Figures 7(a)–(c), the Wind and ACE spectra are systematically higher than the CoDICE-Hi spectra over part of the overlapping energy range. We note that CoDICE-Hi has extremely low counting rates during these intervals, with more than 60% of the measurements being zero in several low-energy channels and the zero-count fraction increasing to more than 80% above ~0.5 MeV. The large fraction of zero-count measurements can reduce the time-averaged CoDICE-Hi intensities relative to Wind and ACE, although their overall time–intensity profiles are generally consistent, as shown in Figure 5. As the shock approaches, the sub-MeV intensities increase and the low-energy spectral differences among the instruments gradually decrease as the CoDICE-Hi counting statistics improve. Upstream anisotropy and differences in instrument viewing geometry may also contribute to the remaining discrepancies. These effects are less important downstream, as shown in Figures 7(d)–(f), where the particle intensities are substantially higher and the cross-instrument energy spectra show much better agreement.

Across the shock and into the downstream region (Figures 7(d)–(e)), the sub-MeV intensities increase by several orders of magnitude relative to the quiet-time levels shown in Figures 7(a)–(b), whereas the higher-energy intensities vary much less. The downstream spectra therefore become increasingly dominated by the low-energy population. The strongest sub-MeV enhancement occurs during 19:00–21:00 UT in Figure 7(e), approximately 5–6 hr after the shock crossing. After the HCS crossing and within the HPS, as shown in Figure 7(f), the sub-MeV intensities decrease, while the several-MeV ion intensities show a slight enhancement. The measurements from the different instruments remain generally consistent during the downstream intervals (Figures 7(d)–(f)). Compared with the reference E^{-2} spectra, the upstream spectra in Figure 7(c) measured by Wind and ACE are roughly consistent with an E^{-2} dependence below ~1 MeV, whereas

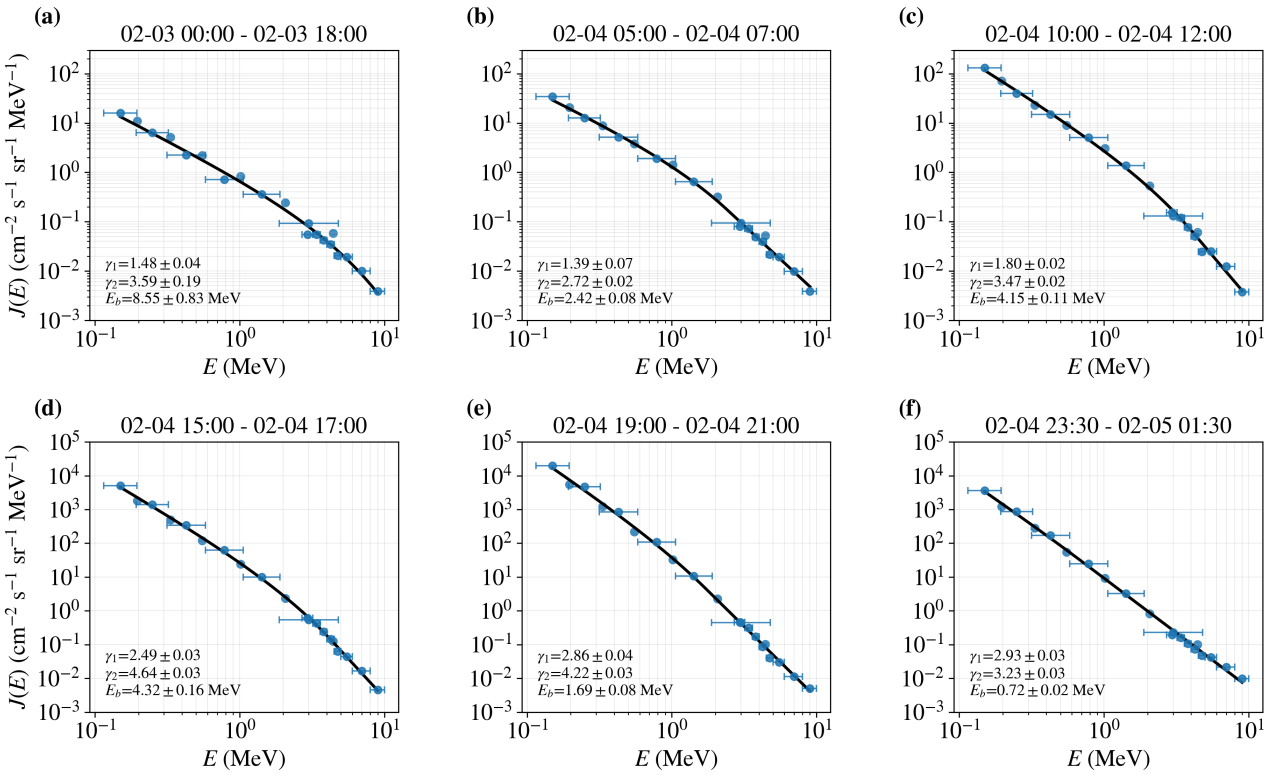


Figure 8. Band-function fits to the energetic-ion differential intensity spectra for the same six intervals shown in Figure 7. Measurements from 3DP/SOSP, ACE/EPAM, and IMAP/HIT are combined to cover ∼0.1–9 MeV. The solid curves show the best-fit Band functions. The fitted low-energy spectral index γ_1, high-energy spectral index γ_2, and break energy E_b, together with their 1σ uncertainties, are listed in each panel.

the downstream sub-MeV energetic-ion spectra become progressively steeper than E^{-2}.

To quantitatively characterize the evolution of the spectral shape, we fit the combined ACE, Wind, and IMAP/HIT spectra using a Band function (D. Band et al. 1993). The differential intensity is expressed as

$$J(E) = \begin{cases} A\left(\frac{E}{E_{\rm ref}}\right)^{-\gamma_1}\exp\left(-\frac{E}{E_0}\right), & E < E_b, \\ A\left[\frac{(\gamma_2-\gamma_1)E_0}{E_{\rm ref}}\right]^{\gamma_2-\gamma_1}\exp(\gamma_1-\gamma_2)\left(\frac{E}{E_{\rm ref}}\right)^{-\gamma_2}, & E \geqslant E_b, \end{cases} \quad (3)$$

where A is the normalization factor, E_0 characterizes the transition between the two spectral regimes, γ_1 and γ_2 are the low- and high-energy spectral indices, respectively, and $E_b = (\gamma_2 - \gamma_1)E_0$ is the break energy. $E_{\rm ref}$ is a fixed reference energy used for normalization.

Figure 8 shows Band-function fits to the energetic-ion spectra for the same six intervals as Figure 7. IMAP/CoDICE-Hi is excluded from the fits because its upstream spectra show systematic differences from those of the other L1 instruments, as discussed above, likely related in part to the large fraction of zero-count measurements near the instrument detection limit. The combined measurements (blue dots) from Wind/3DP/SOSP, ACE/EPAM, and IMAP/HIT show good agreement and are used to characterize the spectral evolution (black curves). We estimate the uncertainties in the fitted Band-function parameters from the covariance matrix of the nonlinear least-squares fit performed in logarithmic space (Z. Liu et al. 2020). Since $E_b = (\gamma_2 - \gamma_1)E_0$ is a derived parameter, its uncertainty is calculated by propagating the full covariance matrix of γ_1, γ_2, and E_0, including the parameter covariances. The resulting 1σ fitting uncertainties in γ_1, γ_2, and E_b are reported in Figure 8.

As shown in Figure 8(a), during the quiet-time interval about 21 hr before the shock crossing, the low-energy spectrum is relatively hard and is approximately described by an $E^{-1.5}$ dependence, corresponding to the v^{-5} velocity distribution often reported for suprathermal ions in the solar wind (L. Fisk & G. Gloeckler 2006; M. Zhang et al. 2019). The fitted break energy, $E_b = 8.55 \pm 0.83$ MeV, lies close to the upper boundary of the measured energy range, and the high-energy spectral index $\gamma_2 = 3.59 \pm 0.19$ should therefore be interpreted cautiously. In Figure 8(b), about 7 hr before the shock crossing, a clearer broken-power-law shape develops, with $\gamma_1 = 1.39 \pm 0.07$ and $E_b = 2.42 \pm 0.08$ MeV. As the shock approaches in Figure 8(c), the low-energy spectrum steepens to $\gamma_1 = 1.8 \pm 0.02$, while the break energy increases to $E_b = 4.15 \pm 0.11$ MeV. The increase in E_b relative to Figure 8(b) is substantially larger than the corresponding 1σ fitting uncertainties, indicating a significant shift of the spectral transition toward higher energies as the shock approaches.

Downstream, the low-energy spectrum becomes substantially softer. Immediately downstream in Figure 8(d), $\gamma_1 = 2.49 \pm 0.03$ and $E_b = 4.32 \pm 0.16$ MeV. The break energy is consistent, within the fitting uncertainties, with that in the preshock interval shown in Figure 8(c), despite the pronounced softening of the low-energy spectral index. Farther downstream, during the maximum low-energy ion intensity in Figure 8(e), γ_1 increases to 2.86 ± 0.04, while E_b decreases

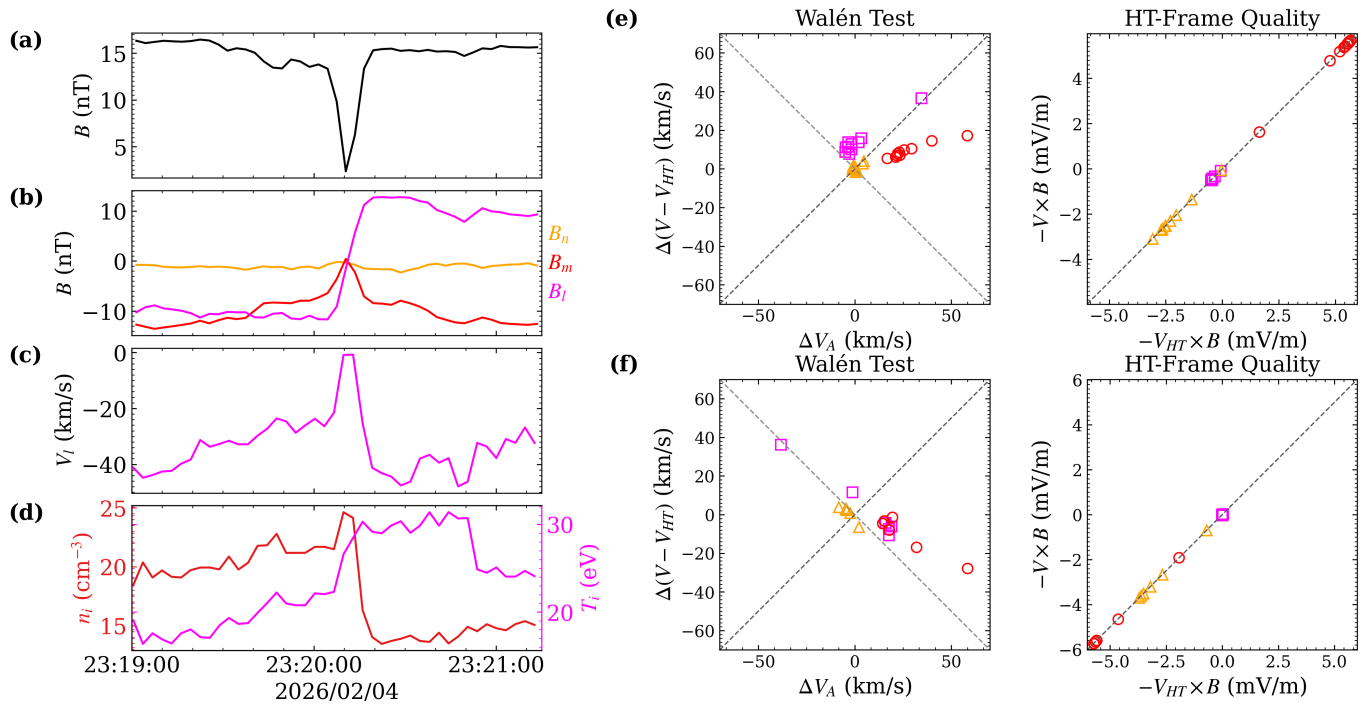


Figure 9. A localized magnetic-reconnection exhaust embedded within the downstream HCS/HPS observed by Wind. (a)–(d) $|B|$, the LMN magnetic-field components, V_L, and plasma density and temperature. (e) and (f) The Walén tests and de Hoffmann–Teller (HT) frame quality at the two boundaries. The magenta squares, red circles, and yellow triangles denote the L, M, and N components, respectively. The opposite Alfvénic signatures and good HT-frame agreement are consistent with a localized reconnection exhaust.

significantly to 1.69 ± 0.08 MeV. Within the HCS/HPS interval in Figure 8(f), the break shifts further downward to $E_b = 0.72 \pm 0.02$ MeV, while $\gamma_1 = 2.93 \pm 0.03$ and $\gamma_2 = 3.23 \pm 0.03$ become more similar, indicating a spectrum approaching a single power law.

The fitted E_b increases during the upstream evolution from Figures 8(b) to (c) and decreases farther downstream from Figures 8(d) to (f), with the changes exceeding the corresponding 1σ fitting uncertainties. Nevertheless, the fitted break energies should be interpreted cautiously when E_b approaches the boundaries of the ∼0.1–9 MeV measurement range, because relatively few data points are available above the break when $E_b \gtrsim 4$ MeV, limiting the constraint on the high-energy spectral component and hence the determination of E_b. This limitation is particularly important in Figure 8(a), where the fitted break lies close to the upper boundary of the measured energy range. The evolution of E_b is therefore best regarded as an indicator of changes in the spectral transition rather than as a precise physical cutoff energy.

5. Localized Reconnection Exhaust in the HPS

While the extended downstream sub-MeV enhancement may partly reflect energy-dependent transport and changing magnetic connectivity to different portions of the structured shock surface (M.-Y. Lo et al. 2026), the disturbed HCS/HPS region may also contain localized structures capable of additional particle energization. As shown in Figure 9, we examine a thin current sheet embedded within the downstream HPS using Wind observations, which provide comparatively high-time-resolution plasma measurements at a cadence of 3 s. The analysis combines minimum variance analysis (MVA), de Hoffmann–Teller (HT) analysis, and Walén tests. The HT frame is determined independently for the intervals 23:19:40–23:20:12 UT and 23:20:12–23:20:30 UT on 2026 February 4. For each interval, we determine a constant velocity, $\boldsymbol{V}_{\rm HT}$, that minimizes $\langle|(\boldsymbol{V} - \boldsymbol{V}_{\rm HT}) \times \boldsymbol{B}|^2\rangle$, where the brackets denote an average over the interval (A. V. Khrabrov & B. U. Ö. Sonnerup 1998). The quality of the HT frame is assessed by comparing $-\boldsymbol{V}_{\rm HT} \times \boldsymbol{B}$ with the convective electric field inferred from the plasma and magnetic-field measurements, $-\boldsymbol{V} \times \boldsymbol{B}$. The magnetic-field magnitude $|B|$ decreases to nearly zero near the center of the current sheet in Figure 9(a). The MVA yields the local LMN basis vectors $\hat{\boldsymbol{L}} = (0.1181, -0.0824, 0.9896)$, $\hat{\boldsymbol{M}} = (-0.5197, 0.8440, 0.1323)$, and $\hat{\boldsymbol{N}} = (-0.8461, -0.5299, 0.0569)$ in geocentric solar ecliptic (GSE) coordinates. As shown in Figure 9(b), a clear reversal of B_L is observed together with a finite guide field B_M comparable in magnitude to B_L. The MVA eigenvalue ratios, $\lambda_L/\lambda_M = 11.5$ and $\lambda_M/\lambda_N = 35.8$, indicate that the minimum variance direction $\hat{\boldsymbol{N}}$, and hence the local current-sheet normal, is well constrained. In Figure 9(c), a localized plasma jet is also observed within the current sheet as a pronounced variation in V_L, accompanied by changes in plasma density and a modest temperature enhancement shown in Figure 9(d).

To determine whether the localized jet is consistent with a reconnection exhaust, we perform Walén tests separately across the two boundaries of the candidate exhaust. In the Walén-test Figures 9(e)–(f), the two dashed diagonals indicate the ideal +1 and −1 Alfvénic relations. Across the first boundary, during 23:19:40–23:20:12 UT, the change in plasma velocity in the HT frame shows an approximately positive Alfvénic relationship with $\Delta V_{\rm A}$, as shown in the left panel of Figure 9(e). Across the second boundary, during 23:20:12–23:20:30 UT, the dominant variations have the opposite Walén sense, as shown in the left panel of Figure 9(f).

The corresponding HT-frame tests in the right panels of Figures 9(e) and (f) show close agreement between the measured convective electric field, $-\boldsymbol{V} \times \boldsymbol{B}$, and that predicted from the derived HT velocity, $-\boldsymbol{V}_{\rm HT} \times \boldsymbol{B}$, indicating that a reasonably well-defined HT frame exists for both intervals. The opposite Alfvénic signatures across the two boundaries, combined with the good HT-frame agreement, are consistent with the spacecraft crossing the two rotational-discontinuity-like boundaries of a localized reconnection exhaust.

The strong magnetic-field rotation and depression, localized plasma jet and heating, well-constrained current-sheet normal, and oppositely directed Alfvénic signatures across the two boundaries are consistent with a localized reconnection exhaust embedded within the disturbed HPS. The presence of such a structure indicates that the postshock HCS/HPS is magnetically complex and contains secondary current sheets and localized reconnection sites. These structures may modify energetic-particle transport through changes in magnetic connectivity and trapping and may also provide localized particle energization (G. P. Zank et al. 2014; J. A. le Roux et al. 2015; O. V. Khabarova & G. P. Zank 2017; L.-L. Zhao et al. 2019b; M. I. Desai et al. 2025; T. D. Phan et al. 2025). However, the present observations do not establish the relative importance of such localized processes compared with shock acceleration and downstream transport.

6. Discussion and Conclusions

In summary, we present a multispacecraft analysis of an IP shock observed near L1. Multispacecraft timing determines the shock normal and propagation speed, while independently derived local shock normals are used to reconstruct the nonplanar shock front, with a characteristic radius of curvature of order $\sim 10^6$ km. Despite variations in the local shock normals among the spacecraft, the shock remains highly quasiperpendicular across the L1 region. The shock is followed by a disturbed downstream region, and about 7.7 hr later the spacecraft encounter an HCS embedded within a broader HPS. The HCS is identified by the magnetic-field-polarity reversal, while the surrounding HPS is primarily characterized by elevated plasma beta and strong magnetic variability. The HCS/HPS is followed by an MC characterized by enhanced magnetic-field strength, smooth field rotation, and low plasma beta.

The energetic-ion observations show a pronounced energy-dependent evolution across the event. Sub-MeV intensities increase well upstream of the shock and remain elevated throughout much of the downstream sheath, whereas ions above $\sim$1 MeV show a weaker extended downstream enhancement and are generally strongest closer to the shock. Such extended downstream enhancements have been reported in previous shock-associated particle events (e.g., D. Lario et al. 2003) and may result from energy-dependent transport and changing magnetic connectivity to different portions of a structured shock surface, which can displace energetic-particle intensity maxima from the local shock crossing (e.g., J. Giacalone & M. Neugebauer 2008; M.-Y. Lo et al. 2026).

The pitch-angle evolution of the sub-MeV ions provides additional constraints on their downstream transport. Pronounced field-aligned streaming develops in the near-upstream region approximately 1 hr before the shock crossing, while downstream the PAD evolves toward a pancake-like distribution centered near 90°. This perpendicular anisotropy persists through much of the downstream sheath, although it becomes broader as the spacecraft approaches the HCS/HPS. The initial development of the pancake-like PAD just downstream of the shock is likely related to the highly quasiperpendicular shock geometry (e.g., I. Richardson & H. Cane 2010), with the enhanced perpendicular component being consistent with SDA. Farther downstream, the coexistence of sustained sub-MeV intensities with a long-lasting but evolving pancake-like PAD suggests that the energetic-ion population continues to be transported through the downstream sheath while its PAD is reshaped by scattering and changes in the local magnetic environment. The pancake-like PAD weakens across the broader HPS and largely disappears after the spacecraft enters the following MC, where the magnetic-field configuration changes substantially.

The upstream sub-MeV spectrum approaches an E^{-2} dependence near the shock, broadly consistent with the test-particle DSA slope expected for a compression ratio of $r \approx 2$. Downstream, the low-energy portion of the spectrum becomes substantially softer, with the spectral slope changing from approximately $E^{-1.8}$ upstream to $E^{-2.5}$–$E^{-2.9}$, while the fitted spectral break shifts toward lower energies. This evolution indicates an increasing dominance of the sub-MeV ion population relative to the higher-energy ions. Energy-dependent transport likely contributes to this spectral softening, as higher-energy particles can diffuse away from the shock more efficiently, reducing their relative intensity farther downstream. Additional energization within the disturbed downstream sheath may also contribute at lower energies through interactions with reconnecting current sheets and other small-scale magnetic structures.

The downstream HCS/HPS introduces additional magnetic complexity. A secondary current sheet embedded within the HPS exhibits a strong magnetic-field depression and rotation, a localized plasma jet, and modest heating, consistent with a localized reconnection exhaust. Although the observed exhaust is unlikely to account for the extended sub-MeV enhancement by itself, it demonstrates that magnetic reconnection occurs within the disturbed HCS/HPS and may provide conditions for particle energization. Overall, the observations favor a picture in which the energetic-ion population is strongly influenced by the shock, while its subsequent downstream evolution is shaped by energy-dependent transport. Localized downstream processes, such as magnetic reconnection and interactions with current-sheet-like structures, may provide an additional contribution to the sub-MeV population.

Acknowledgments

This work is funded by the IMAP mission as part of NASA's Solar Terrestrial Probes (STP) Program (80GSFC19C0027). We acknowledge partial support from the NSF EPSCoR RII-Track-1 cooperative agreement OIA-1655280, NSF award 2442628, and NASA awards 80NSSC20K1783, 80NSSC23K0415, and 80NSSC25K7750. IMAP magnetometer operations are funded by the UK Space Agency (grant UKRI2494). T.H. is supported by STFC grant UKRI1202. We acknowledge the use of measurements from Wind, ACE, IMAP, DSCOVR, and SOLAR-1. The Wind, ACE, IMAP, and DSCOVR data products used in this study are obtained from NASA's Coordinated Data Analysis Web (CDAWeb; https://cdaweb.gsfc.nasa.gov/). The SOLAR-1 magnetic-field measurements used in this study are pre-provisional MAG data made available

by the SWFO/SOLAR-1 team. SOLAR-1 operational MAG data are publicly accessible through the NOAA Space Weather Prediction Center (SWPC; https://www.spaceweather.gov/products/solar-wind). Upon completion of validation, the finalized SOLAR-1 datasets are available through the NOAA/National Centers for Environmental Information (NCEI) Space Weather Portal (SPOT; https://www.ncei.noaa.gov/products/space-weather).

ORCID iDs

L.-L. Zhao https://orcid.org/0000-0002-4299-0490
X. Zhu https://orcid.org/0000-0002-1541-6397
Y. Jiao https://orcid.org/0009-0004-4832-0895
Z. Jin https://orcid.org/0000-0001-8747-7407
N. M. Subashchandar https://orcid.org/0009-0008-2509-9330
G. P. Zank https://orcid.org/0000-0002-4642-6192
A. Silwal https://orcid.org/0000-0001-6286-2106
D. J. McComas https://orcid.org/0000-0001-6160-1158
S. Raptis https://orcid.org/0000-0002-4381-3197
J. Giacalone https://orcid.org/0000-0002-0850-4233
M. A. Dayeh https://orcid.org/0000-0001-9323-1200
M. J. Starkey https://orcid.org/0000-0001-7514-6571
K. Ogasawara https://orcid.org/0000-0002-0429-8380
S. T. Hart https://orcid.org/0000-0003-0508-4912
M. E. Cuesta https://orcid.org/0000-0002-7341-2992
L. Y. Khoo https://orcid.org/0000-0003-0412-1064
D. Turner https://orcid.org/0000-0002-2425-7818
J. S. Rankin https://orcid.org/0000-0002-8111-1444
T. S. Horbury https://orcid.org/0000-0002-7572-4690
S. A. Livi https://orcid.org/0000-0002-4149-7311
E. R. Christian https://orcid.org/0000-0003-2134-3937
J. G. Mitchell https://orcid.org/0000-0003-4501-5452
M. Gkioulidou https://orcid.org/0000-0001-9979-2164
R. B. Torbert https://orcid.org/0000-0001-7188-8690
D. Vassiliadis https://orcid.org/0009-0007-6554-3611

References

Adhikari, L., Khabarova, O., Zank, G. P., & Zhao, L.-L. 2019, ApJ, 873, 72
Ala-Lahti, M., Pulkkinen, T. I., Suni, J., et al. 2025, ApJL, 994, L30
Axford, W. I., Leer, E., & Skadron, G. 1977, ICRC, 11, 132
Band, D., Matteson, J., Ford, L., et al. 1993, ApJ, 413, 281
Battarbee, M., Dalla, S., & Marsh, M. S. 2018, ApJ, 854, 23
Bell, A. R. 1978, MNRAS, 182, 147
Blandford, R. D., & Ostriker, J. P. 1978, ApJL, 221, L29
Burlaga, L., Lepping, R., & Jones, J. 1990, GMS, 58, 373
Burt, J., & Smith, B. 2012, in 2012 IEEE Aerospace Conf. (IEEE), 1
Christian, E. R., Mitchell, J. G., Bruno, A., et al. 2026, SSRv, 222, 23
Colburn, D. S., & Sonett, C. P. 1966, SSRv, 5, 439
Crooker, N., Huang, C.-L., Lamassa, S., et al. 2004, JGRA, 109, A03107
Cuesta, M. E., Horbury, T. S., Rankin, J. S., et al. 2026, ApJS, 288, 3
Dayeh, M. A., Desai, M. I., Ogasawara, K., et al. 2026, ApJS, submitted
Decker, R. B. 1983, JGRA, 88, 9959
Desai, M., & Giacalone, J. 2016, LRSP, 13, 3
Desai, M. I., Drake, J. F., Phan, T., et al. 2025, ApJL, 985, L38
Desai, M. I., Mitchell, D. G., McComas, D. J., et al. 2022, ApJ, 927, 62
Ding, Z., Wimmer-Schweingruber, R. F., Chen, Y., et al. 2025, A&A, 701, A123
Drake, J. F., Cassak, P., Shay, M., Swisdak, M., & Quataert, E. 2009, ApJL, 700, L16
Drake, J. F., Swisdak, M., Che, H., & Shay, M. A. 2006, Natur, 443, 553
Dresing, N., Gómez-Herrero, R., Heber, B., et al. 2014, A&A, 567, A27
Dresing, N., Rodríguez-García, L., Jebaraj, I. C., et al. 2023, A&A, 674, A105
Drury, L. O. 1983, RPPh, 46, 973
Du, S., Li, H., Skoug, R., Steinberg, J., & Guo, F. 2025, FrASS, 12, 1664531
Erdös, G., & Balogh, A. 1994, in IAU Colloq. 142, Particle Acceleration Phenomena in Astrophysical Plasmas (Cambridge Univ. Press), 553
Fisk, L., & Gloeckler, G. 2006, ApJL, 640, L79
Fisk, L. A., & Gloeckler, G. 2007, PNAS, 104, 5749
Giacalone, J. 2012, ApJ, 761, 28
Giacalone, J., & Burgess, D. 2010, GeoRL, 37, L19104
Giacalone, J., Burgess, D., Bale, S. D., et al. 2021, ApJ, 921, 102
Giacalone, J., & Neugebauer, M. 2008, ApJ, 673, 629
Gold, R. E., Roelof, E. C., Krimigis, S., et al. 2022, ACE Electron Proton Alpha Monitor (EPAM) 12-sec Level 2 Data, Space Physics Data Facility, doi:10.48322/JQJ0-VN49
Gosling, J. T., McComas, D. J., Skoug, R. M., & Smith, C. W. 2006, GeoRL, 33, L17102
Gosling, J. T., Skoug, R. M., Haggerty, D. K., & McComas, D. J. 2005a, GeoRL, 32, L14113
Gosling, J. T., Skoug, R. M., McComas, D. J., & Smith, C. W. 2005b, GeoRL, 32, L05105
Guo, X., Yang, L., Wang, L., & Ma, Q. 2026, ApJL, 1006, L35
Hakobyan, H., Petropoulou, M., Spitkovsky, A., & Sironi, L. 2021, ApJ, 912, 48
Horbury, T. S., O'Brien, H. L., Greenaway, C., et al. 2026, SSRv, 222, 44
Jokipii, J. R. 1966, ApJ, 146, 480
Jokipii, J. R. 1987, ApJ, 313, 842
Khabarova, O., Zank, G. P., Li, G., et al. 2015, ApJ, 808, 181
Khabarova, O. V., & Zank, G. P. 2017, ApJ, 843, 4
Khrabrov, A. V., & Sonnerup, B. U. Ö. 1998, ISSIR, 1, 221
Kilpua, E. K. J., Good, S. W., Dresing, N., et al. 2021, A&A, 656, A8
Klein, L., & Burlaga, L. 1982, JGR, 87, 613
Koval, A. 2026, DSCOVR Fluxgate Magnetometer (MAG) Definitive Magnetic Field, 1 second data, Space Physics Data Facility, doi:10.48322/2YVC-9N97
Koval, A., Lepping, R. P., & Szabo, A. 2023, Wind Magnetic Field Investigation (MFI) Composite Data in RTN Coordinates, Space Physics Data Facility, doi:10.48322/S1D0-5Q92
Lario, D., Ho, G. C., Decker, R. B., et al. 2003, AIPC, 679, 640
Lario, D., Hu, Q., Ho, G. C., et al. 2005, ESASP, 592, 81
le Roux, J. A., Zank, G. P., Webb, G. M., & Khabarova, O. 2015, ApJ, 801, 112
le Roux, J. A., Zank, G. P., Webb, G. M., & Khabarova, O. V. 2016, ApJ, 827, 47
Lee, M. A. 2005, ApJS, 158, 38
Lin, R. P., Bale, S. D., & Wilson, L. B., III 2021a, Wind 3DP PESA Moments Data, Space Physics Data Facility, doi:10.48322/S8E6-AW08
Lin, R. P., Bale, S. D., & Wilson, L. B., III 2021b, Wind 3DP SST Open Proton Omnidirectional Fluxes, Space Physics Data Facility, doi:10.48322/WKK0-Y398
Lin, R. P., Bale, S. D., & Wilson, L. B., III 2021c, Wind 3DP SST Open Proton Energy-Angle Distributions, Space Physics Data Facility, doi:10.48322/YW1C-YF03
Lin, R. P., Bale, S. D., Wilson, L. B., III, & Schroeder, P. 2021d, Wind 3DP EESA-LOW Electron Pitch-Angle Distributions, Space Physics Data Facility, doi:10.48322/KESF-RE26
Liou, K., & Wu, C.-C. 2024, ApJ, 966, 16
Liu, Z., Wang, L., & Guo, X. 2022, ApJ, 935, 39
Liu, Z., Wang, L., Wimmer-Schweingruber, R. F., Krucker, S., & Mason, G. M. 2020, JGRA, 125, e28702
Livi, S. A., Desai, M. I., Ogasawara, K., et al. 2025, SSRv, 222, 1
Lo, M.-Y., Guo, F., Giacalone, J., et al. 2026, ApJ, 1002, 10
Malandraki, O., Khabarova, O., Bruno, R., et al. 2019, ApJ, 881, 116
Mallet, A., Klein, K., Chandran, B. D. G., Ervin, T., & Bowen, T. A. 2026, JPlPh, 92, E13
Matthaeus, W., Dasso, S., Weygand, J., et al. 2005, PhRvL, 95, 231101
Matthaeus, W. H., Qin, G., Bieber, J. W., & Zank, G. P. 2003, ApJL, 590, L53
McComas, D. J., Christian, E. R., Schwadron, N. A., et al. 2025, SSRv, 221, 100
Moreland, K., Dayeh, M., Li, G., et al. 2023, ApJ, 956, 107
Murtas, G., Li, X., & Guo, F. 2024, ApJ, 974, 28
Neugebauer, M., & Giacalone, J. 2005, JGRA, 110, A12106
Odstrčil, D., Dryer, M., & Smith, Z. 1996, JGR, 101, 19973
Oka, M., Phan, T.-D., Krucker, S., Fujimoto, M., & Shinohara, I. 2010, ApJ, 714, 915
Parker, E. N. 1965, P&SS, 13, 9
Paschmann, G., & Daly, P. W. 1998, Analysis Methods for Multi-Spacecraft Data, ISSI Scientific Reports Series SR-001, ESA/ISSI
Petrosian, V. 2012, SSRv, 173, 535
Phan, T. D., Lavraud, B., Halekas, J. S., et al. 2021, A&A, 650, A13

Phan, T. D., Romeo, O. M., Drake, J. F., et al. 2025, ApJ, 986, 209
Rankin, J. S., McComas, D. J., Alimaganbetov, M., et al. 2025, SSRv, 221, 108
Raptis, S., Turner, D. L., Trotta, D., et al. 2026, ApJS, submitted
Richardson, I., & Cane, H. 2010, JGRA, 115, A07103
Ruffolo, D. 1995, ApJ, 442, 861
Russell, C. T., Mellott, M. M., Smith, E. J., & King, J. H. 1983, JGR, 88, 4739
Silwal, A., Zhao, L., Zank, G. P., et al. 2024, ApJ, 972, 168
Skoug, R. M., Schultz, T. B., Venhaus, D. M., et al. 2026, SSRv, 222, 45
Smith, C., & Ness, N. 2022, ACE Magnetic Field (MAG) Geocentric Solar Ecliptic, GSE, and Geocentric Solar Magnetospheric, GSM, Coordinates, Level 2 (H3), 1 s Data, Space Physics Data Facility, doi:10.48322/7XYH-4Z44
Smith, Z., Odstrcil, D., & Dryer, M. 1998, JGR, 103, 20581
Sours, S. C., Doran, P. L., Verma, A. K., Rimlinger, T. J., & McNeil, A. J. 2026, 2026 AAS/AIAA Astrodynamics Specialist Conf. https://ntrs.nasa.gov/citations/20260002159
Stone, E. C., Frandsen, A. M., Mewaldt, R. A., et al. 1998, SSRv, 86, 1
Torbert, R., Rodriguez, J., Loto'aniu, P., et al. 2026, NOAA Space Weather Follow-on Lagrange 1 (SOL-1) MAG L2 Retrospective Data in Daily Aggregations, NOAA National Centers for Environmental Information, doi:10.25921/stzs-xs74
Trotta, D., Vuorinen, L., Hietala, H., et al. 2022, FrASS, 9, 1005672
Vassiladis, D. 2026, GSICS Quart., 19, 1
Wilson, L. B., III, Brosius, A. L., Gopalswamy, N., et al. 2021, RvGeo, 59, e2020RG000714
Winterhalter, D., Smith, E., Burton, M., Murphy, N., & McComas, D. 1994, JGR, 99, 6667
Wu, C.-C., Liou, K., Vourlidas, A., et al. 2016, JGRA, 121, 56
Yang, L., Berger, L., Wimmer-Schweingruber, R. F., et al. 2020, ApJL, 888, L22
Yang, L., Heidrich-Meisner, V., Berger, L., et al. 2023, A&A, 673, A73
Yang, L., Heidrich-Meisner, V., Wang, W., et al. 2024, A&A, 686, A132
Yang, L., Kollhoff, A., Heidrich-Meisner, V., et al. 2025a, A&A, 700, L7
Yang, L., Li, X.-Y., Heidrich-Meisner, V., et al. 2025b, A&A, 695, A270
Yang, L., Wang, L., Li, G., et al. 2018, ApJ, 853, 89
Yang, L., Wang, L., Li, G., et al. 2019, ApJ, 875, 104
Zank, G. P., Hunana, P., Mostafavi, P., et al. 2015, ApJ, 814, 137
Zank, G. P., le Roux, J. A., Webb, G. M., Dosch, A., & Khabarova, O. 2014, ApJ, 797, 28
Zhang, M., Qin, G., & Rassoul, H. 2009, ApJ, 692, 109
Zhang, M., Zhao, L., von Steiger, R., et al. 2019, ApJ, 871, 60
Zhao, L.-L., Zank, G., Hu, Q., et al. 2019a, ApJ, 886, 144
Zhao, L.-L., Zank, G. P., Chen, Y., et al. 2019b, ApJ, 872, 4
Zhao, L.-L., Zank, G. P., Khabarova, O., et al. 2018, ApJL, 864, L34
Zharkova, V. V., & Khabarova, O. V. 2012, ApJ, 752, 35
Zhu, X., Yang, L., Zhao, L., et al. 2026, A&A, 706, A356